

Scaling Up Purcell-Enhanced Self-Assembled Nanoplasmonic Perovskite Scintillators into the Bulk Regime

Michal Makowski,^{1, a)} Wenzheng Ye,^{2, 3} Dominik Kowal,¹ Francesco Maddalena,^{2, 3} Somnath Mahato,¹ Yudhistira Tirtayasri Amrillah,⁴ Weronika Zajac,^{1, 5} Marcin Eugeniusz Witkowski,⁶ Konrad Jacek Drozdowski,⁶ Nathaniel,⁴ Cuong Dang,^{2, 3} Joanna Cybinska,^{1, 5} Winicjusz Drozdowski,⁶ Ferry Anggoro Ardy Nugroho,⁴ Christophe Dujardin,^{7, 8} Liang Jie Wong,^{2, 3, b)} and Muhammad Danang Birowosuto^{1, c)}

¹⁾ *Lukasiewicz Research Network - PORT Polish Center for Technology Development, Wroclaw, 54-066, Poland*

²⁾ *CINTRA (CNRS-International-NTU-THALES Research Alliance), IRL 3288 Research Techno Plaza, 50 Nanyang Drive, Border X Block, Level 6, Singapore 637553, Singapore*

³⁾ *School of Electrical and Electronic Engineering, Nanyang Technological University, Singapore 639798, Singapore*

⁴⁾ *Department of Physics, Faculty of Mathematics and Natural Sciences, Universitas Indonesia, 16424 Depok, Indonesia*

⁵⁾ *Faculty of Chemistry, University of Wroclaw, Wroclaw, 50-383, Poland*

⁶⁾ *Institute of Physics, Faculty of Physics, Astronomy, and Informatics, Nicolaus Copernicus University in Torun, Torun, 87-100, Poland*

⁷⁾ *Universite Claude Bernard Lyon 1, Institut Lumiere Matiere UMR 5306 CNRS, 10 rue Ada Byron, Villeurbanne, 69622, France*

⁸⁾ *Institut Universitaire de France (IUF), 1 rue Descartes, Paris Cedex 05, 75231, France*

(Dated: 28 November 2024)

Scintillators, which convert high-energy radiation into detectable photons, play a crucial role in medical imaging and security applications. The enhancement of scintillator performance through nanophotonics and nanoplasmonics, specifically using the Purcell effect, has shown promise but has so far been limited to ultrathin scintillator films due to the localized nature of this effect. In this study, we present a method to extend nanoplasmonic scintillators to the bulk regime. By integrating 100-nm-size plasmonic spheroid and cuboid nanoparticles with perovskite scintillator nanocrystals, we enable nanoplasmonic scintillators to function effectively within bulk-scale devices. We experimentally demonstrate power and decay rate enhancements of up to (3.20 ± 0.20) and (4.20 ± 0.31) fold for plasmonic spheroid and cuboid nanoparticles, respectively, in a 5-mm thick CsPbBr₃ nanocrystal-polymer scintillator at RT. Theoretical modeling further predicts similar enhancements of up to (2.63 ± 0.79) and (5.62 ± 1.71) fold for the same nanoparticle shapes and dimensions. These findings provide a viable pathway for using nanoplasmonics to enhance bulk scintillator devices, advancing radiation detection technology.

Keywords: Purcell effect, scintillation, nanocrystals

^{a)}Electronic mail: michal.makowski@port.lukasiewicz.gov.pl

^{b)}Electronic mail: liangjie.wong@ntu.edu.sg

^{c)}Electronic mail: muhammad.birrowosuto@port.lukasiewicz.gov.pl

I. INTRODUCTION

The development of high-performance scintillating materials has remained a priority due to their applications in bioimaging¹ and various industrial technologies². Following Roentgen's discovery of X-rays³, researchers have pursued faster and brighter scintillators by investigating new materials⁴ and enhancing crystal quality. These advancements often involve modifying the emitting-center properties using lanthanide⁵ and transition metal activators⁶. More recently, nanoscale scintillators, particularly nanocrystals (NCs), have gained attention as they offer unique pathways to improve luminescent yield and decay times at room temperature (RT) comparing their bulk associates^{7,8}. However, these intrinsic material properties alone are not the sole determinants of scintillator performance. Increasingly, nanophotonic and nanoplasmonic techniques⁹⁻¹¹, such as the Purcell effect, are being explored to further enhance emission characteristics by modifying the local density of optical states (LDOS)¹¹⁻¹⁶. By optimizing the LDOS, the Purcell effect can significantly amplify radiative decay rates, potentially increasing scintillation efficiency.

Whereas single-crystal scintillators like Cerium doped Lutetium Oxyorthosilicate and Lanthanum Bromide, Thallium doped Sodium and Cesium Iodides, and Bismuth Germanate are commonly used in medical imaging applications operating in counting regime, including positron emission tomography (PET)¹⁷, the class of perovskite scintillators has emerged as promising materials in their own right¹⁸⁻²⁰. Perovskites offer several advantages that make them attractive alternatives to traditional single-crystal scintillators. Notably, perovskite light yields are in the range of tens of photons per keV (ph/keV), comparable to or even surpassing those of established materials. Additionally, perovskites exhibit fast decay times of under 10 nanoseconds, which enhances the timing resolution of imaging systems. The fabrication processes for perovskite materials are often simpler and thus more cost-effective than those for traditional single-crystal scintillators. Finally, the tunability of perovskite materials allows for the optimization of their scintillation properties through compositional adjustments, potentially leading to new scintillator designs tailored for specific imaging requirements¹¹. However, just like other methods that use nanophotonics to enhance scintillator properties, the use of plasmonic thin films results in only a limited region of scintillator material benefiting the Purcell enhancement. This is due to the typically localized nature of the Purcell effect. The challenge remains as to how these enhancements can be scaled to

benefit bulk scintillators, whose thickness can be as large as millimeters in scale^{11,13–16}.

In this work, we overcome this challenge, demonstrating the possibility of realizing nanoplasmonic Purcell enhancement in bulk scintillator materials, by embedding CsPbBr₃^{21,22} perovskite NCs with silver (Ag) nanoparticles (NPs) in a polydimethylsiloxane (PDMS) matrix, creating stable, bright, and scalable scintillating materials suitable for medical and security imaging applications. Ag is selected because it can provide highest enhancements and lower losses for green emission of our NCs¹¹. This hybrid system leverages the Purcell effect, wherein the Ag NPs modify the LDOS, amplifying the light yield and decay rate of CsPbBr₃ NCs without thickness limitations. The concept from nano to bulk was also demonstrated by Förster-resonance-energy-transfer CsPbBr₃ scintillators²³ but our concept is more robust for large area while providing large enhancements. By tuning the interaction between Ag spheroid (SNPs) and cuboid NPs (CNPs) and CsPbBr₃ NCs, this work proposes an original route based on two configurations for enhancing scintillation in large-scale systems, achieving intensified luminescence and faster decay dynamics than previously reported thin-film configurations^{11,13–16}.

The Purcell effect in our experiment is quantified by comparing the luminescence intensity (emitted power, P) and decay time (inverse decay rate, Γ) ratios between CsPbBr₃ NCs dispersed within Ag NP-PDMS composite systems and those in pure PDMS matrices, denoted by a superscript o . The Purcell factor F_p , describing this enhancement, is defined as²⁴:

$$F_p \sim \frac{P}{P^o} \sim \frac{\Gamma}{\Gamma^o} \quad (1)$$

where the ratios Γ/Γ^o and P/P^o both express F_p , depending on the quantum efficiency (QE) of the CsPbBr₃ NCs^{25,26}. To relate F_p to the LDOS, one can further express the Γ/Γ^o ratio using a classical dipole model of the electric Green dyadic $\mathbb{G}^{\mathbb{E}}(\mathbf{r}_s, \mathbf{r}'_s, \omega_{eg})$:

$$\frac{\Gamma}{\Gamma^o} = \frac{6\pi c}{\omega_{eg}} \text{Im} [\mathbf{u} \cdot \mathbb{G}^{\mathbb{E}}(\mathbf{r}_s, \mathbf{r}_s, \omega_{eg})] \quad (2)$$

where ω_{eg} is the Bohr frequency, \mathbf{r}_s is the emitter position, and c is the speed of light. To compute P/P^o , a substitution of ω_{eg} with the frequency of one of the eigenmodes ω is employed²⁴.

Although the Ag NP systems used here are randomly distributed, their interactions can be approximated by modeling a single NP if all NCs and Ag NPs are 100% coupled together or coupling efficiency (C_{coup}) is 100%. Multiple scattering also minimally influences average

decay rate statistics in these disordered systems if the scattering strength is low enough due to the lower index contrast between the medium (PDMS) and the scatterers (Ag NPs) than that between the air and Ag NPs^{27,28}. The multiple-scattering approximation, however, affects only the distribution tail²⁹ and it does not present in our experiments or previous model of ensemble FRET scintillator systems²³. Thus, the Purcell factor of our scintillators can be derived using previous studies of a superemitter, a hybrid system of emitters and plasmonic NPs^{30,31}. For a single CsPbBr₃ NC coupled to a single Ag NP, F_p is given by³²:

$$F_p = \frac{3}{4\pi^2} \lambda_{eg}^3 Q \left(\frac{1}{V} \right) = \frac{6\pi c^3}{\omega_{eg}^3} Q \left(\frac{\max(\epsilon|E|^2)}{\int \epsilon|E|^2 d^3\mathbf{r}} \right) \quad (3)$$

where $\lambda_{eg} = 2\pi c/\omega_{eg}$ and Q is the quality factor of the Ag NP. The parameters Q and mode volume V depend on the NP details, such as SNPs and CNPs, as solved analytically in Supporting Information and Supporting Fig. S1. For plasmonic F_p calculations, V has a greater impact than Q due to typically low Q values (under ten)³². To determine V , the integral over the energy density is calculated, $(\text{Re}\{\epsilon\} + 2\omega\text{Im}\{\epsilon\}\gamma)|E|^2$ ³³. This approach fits well with the Drude model, $\epsilon = 1 - \omega_p^2/\omega(\omega + i\gamma)$, where ω_p and γ denote the plasmonic mode frequency and damping rate for Ag, respectively³². From the description in Eq. 3, F_p is strongly influenced by the maximum energy density in the integral, making it sensitive to sharp NP geometries³³. Structures like CNPs, which feature sharp edges, achieve significantly higher F_p values than SNPs due to these geometric effects³⁴⁻³⁶.

This study examines the intricate interactions between CsPbBr₃ NCs and Ag NPs in a PDMS matrix, focusing on the impact of Ag NP geometry on Purcell enhancements. The analysis integrates experimental findings with theoretical insights and FDTD simulations, incorporating corrections for QE and C_{coup} based on emitter and microscopy characterizations, and compares theoretical predictions with experimental results. Photoluminescence (PL) studies reveal an integrated intensity enhancement of $P_{\text{PL}}/P_{\text{PL}}^o$ at (4.10 ± 0.20) fold at room temperature (RT). Furthermore, time-resolved PL (TRPL) measurements show a significant reduction in the fastest decay time constant, dropping from (0.99 ± 0.03) ns to (0.61 ± 0.04) ns, yielding a maximum overall decay rate ratio $\Gamma_{\text{PL}}/\Gamma_{\text{PL}}^o$ of (4.20 ± 0.31) fold. For X-ray luminescence (XL), peak enhancements reach (1.92 ± 0.13) fold in $P_{\text{XL}}/P_{\text{XL}}^o$ and (2.08 ± 0.06) fold in $\Gamma_{\text{XL}}/\Gamma_{\text{XL}}^o$. Those values are largely consistent with the theoretical enhancements, with CNP-doped samples consistently achieving the highest values. This confirms the Purcell-effect origins while also highlighting the limitations of observational

methods¹¹. Crucially, our Purcell-enhanced scintillator system is designed with a millimeter-scale thickness, addressing the constraints of thin-layer designs. This advancement paves the way for its application in high-energy radiation fields, such as PET and photon-counting computed tomography (PCCT)³⁷.

II. RESULTS

The successful demonstration of the Purcell effect with a single plasmonic nanoparticle critically depends on accurately positioning the emitter - maintaining close proximity to the nanoparticle without making direct contact with its metal surface. High-quality plasmonic NPs are commonly coated with a 5 nm thick poly(vinylpyrrolidone) (PVP) layer acting as a surfactant, facilitating various light-matter interactions, from weak to strong coupling^{38,39}. Ag NPs were selected over Gold (Au) NPs due to their substantially lower optical losses, which prior studies have shown to yield superior Purcell enhancements in Ag-based nanoplasmonic systems, compared to Au-based systems¹¹. Schematic diagrams of NC and NC-NP scintillators are presented in Figs. 1a and b, respectively. Transmission Electron Microscopy (TEM) was used to assess the Ag NPs' size, revealing diameters of (100 ± 8) nm for SNPs and side lengths of (100 ± 10) nm for CNPs (Figs. 1c and d, respectively). Fig. 1e shows an image of the synthesized samples following the PDMS fabrication under ambient conditions, while Fig. 1f depicts the samples under UV lamp excitation. Although the side surfaces of the fabricated cylindrical samples appear slightly rough to the eye, it is not critical in the frame of the scintillation purpose. At first sight, the sample with CNPs is the brightest. For their dimension, the samples were measured to have a diameter ϕ of 10 mm and a thickness of 5 mm. In theory, such thickness is adequate for all samples to fully absorb high-energy radiation within the range of 10 to 50 keV; see Supporting Fig. S2.

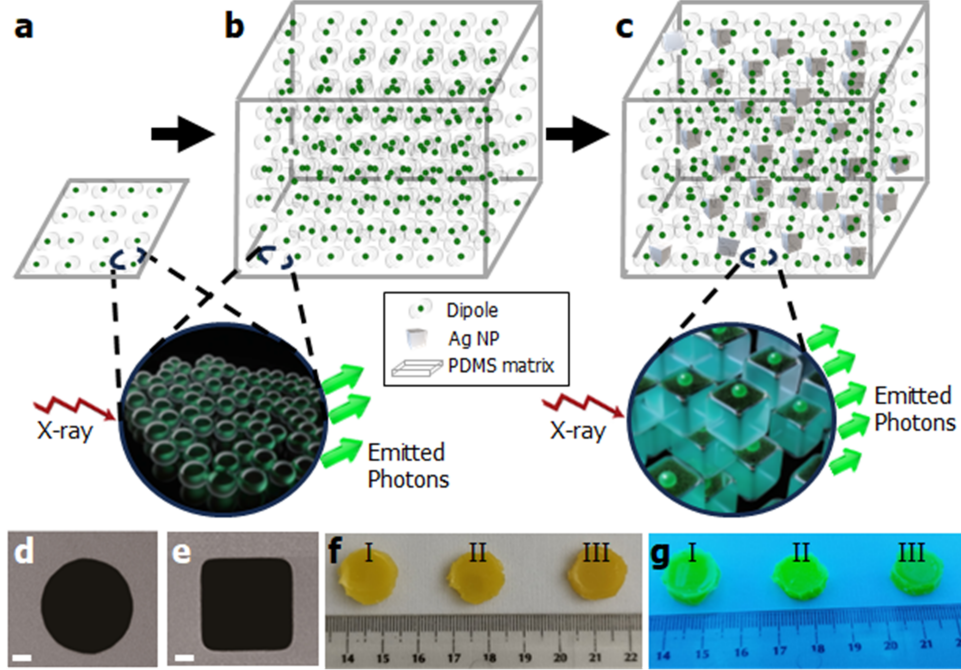


FIG. 1. **Nanoplasmonic scintillators with metal nanoparticles.** **a,b,c**, Schematic descriptions of available CsPbBr₃ nanocrystals (NCs) thin films (**a**), our concept of CsPbBr₃ NCs (**b**) and CsPbBr₃ NCs sample co-doped with silver nanoparticles (Ag NPs) (**c**) embedded into polydimethylsiloxane (PDMS) matrix. The replication and the shortening of the light green arrows indicate a scintillation light yield increase and a decay time shortening, respectively. The sample with NPs shows brightest NCs inside the matrix. **d,e**, High-resolution transmission electron microscopy (TEM) images of individual spheroid (SNPs) (**d**) and cuboid nanoparticles (CNPs) (**e**) (white scale bar: 20 nm). **f,g**, Images of the synthesized samples, captured under ambient conditions (**f**) and UV lamp excitation. (**g**), highlighting the distinct brightnesses of CsPbBr₃ + SNPs (**I**), and CsPbBr₃ + CNPs (**II**), and pure CsPbBr₃ (**III**).

To visualize the attachment of CsPbBr₃ NCs with Ag NPs and investigate the shape and size of single NCs, atomically resolved TEM measurements were performed (Fig. 2). Considering the highly beam-sensitive nature of perovskites, the CsPbBr₃ NCs are characterized by low-dose aberration-corrected scanning TEM high-angle-annular dark-field (STEM-HAADF) imaging operated at 300 kV with a screen current of ~ 20 pA⁴⁰. As can be seen at the low magnification TEM images, the CsPbBr₃ NCs are well attached with Ag NPs and uniformly distributed on the Ag NP surface (Fig. 2a). The average side lengths of the CsPbBr₃ NCs are calculated to be (7.30 ± 0.20) nm and (6.76 ± 0.20) nm while the

atomic distance of Pb-Pb atoms is 0.59 nm (Fig. 2b and Supporting Fig. S3). To verify the crystallinity and the growth of the NCs, Fast Fourier Transform patterns derived from Fig. 2b are shown in Fig. 2c. The well-defined diffraction spots indicate the high crystallinity of CsPbBr₃ NCs. The indexed diffraction spots of the (100) and (110) crystal planes along the [001] zone axis also indicate the cubic phase in CsPbBr₃⁴¹. Subsequently, to visualize the Ag NPs, the well-resolved lattice fringes (Fig. 2d) with an interplanar spacing of 0.40 nm corresponds to the (100) crystal faces of Ag-Ag atoms (Supporting Fig. S3)⁴². Verification of the chemical composition at the atomic scale can provide direct evidence for the determination of the materials' structures and chemical information and has been demonstrated with energy-dispersive X-ray spectra (EDS). The region for EDS spectral imaging is displayed in Fig. 2e with the STEM-HAADF image. Elemental maps shown in Figs. 2f-i were extracted from EDS spectral images with selected energy windows for Br, Cs, Pb, and Ag, respectively. Consequently, calculations were performed to estimate the amount of CsPbBr₃ NCs coupled on the surfaces of Ag NPs. EDS images showing the overlap between Ag and Pb or Br elements were analyzed using the Sørensen-Dice similarity method⁴³ and the coupling percentage for both Ag NP-doped samples is approximated to be $C_{coup} = (70 \pm 8) \%$ (Supporting Fig. S3).

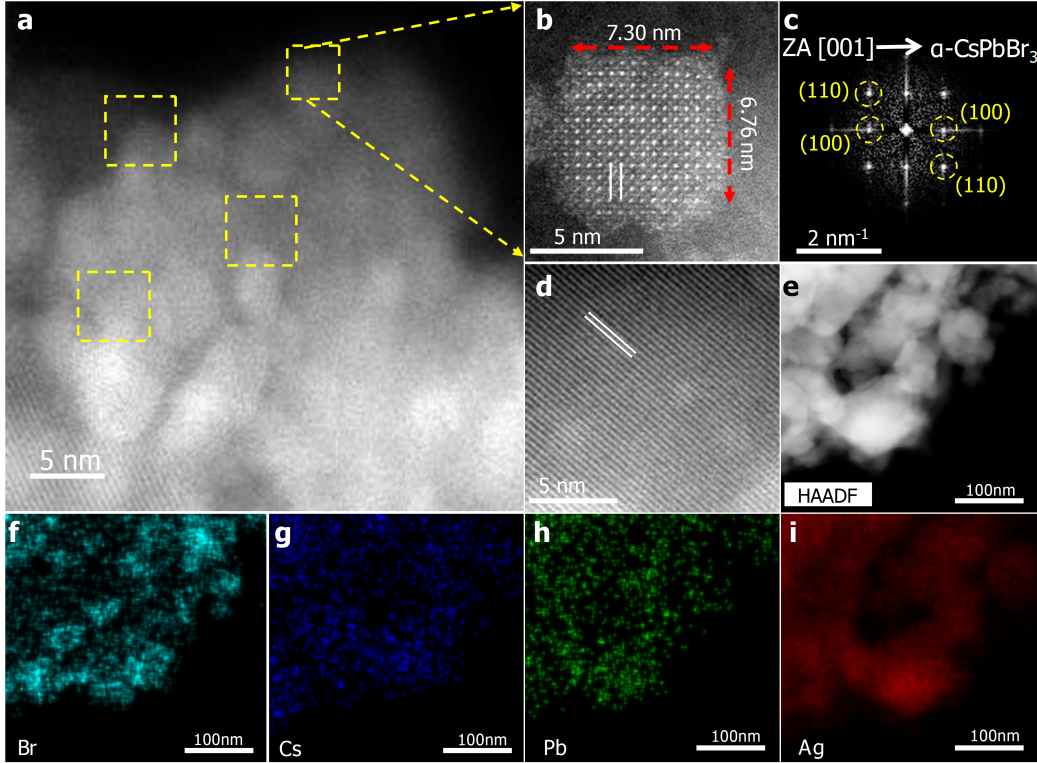


FIG. 2. Morphology of Ag CNPs surrounded by myriad CsPbBr₃ NCs. **a**, Scanning TEM high-angle annular dark-field (STEM-HAADF) image of the Ag CNP embedded within the CsPbBr₃ NCs. Areas marked with yellow squares indicate regions selected for energy-dispersive X-ray analysis. **b,c**, Atomic resolution STEM-HAADF image with the lattice spacing of 0.59 nm shown as white parallel lines (**b**) of the CsPbBr₃ NCs, with corresponding Fast Fourier Transform image (**c**) revealing diffraction spots indexed with (100) and (110) planes, confirming the cubic phase of CsPbBr₃. **d**, High-resolution STEM-HAADF image with the lattice spacing of 0.40 nm from the corresponding Ag atoms shown as white parallel lines. **e**, A low magnification STEM-HAADF image of Ag embedded with CsPbBr₃ NCs. **f-i**, X-ray elemental maps for Br (**f**), Cs (**g**), Pb (**h**), and Ag (**i**), showcasing the compositional distribution in this hybrid system.

To clarify the role of Ag NPs in enhancing emitter characteristics and to validate our Purcell enhancement strategy, the FDTD simulations for CsPbBr₃ NCs attached to single Ag NP were performed. These simulations were configured with a 5-nm emitter-NP separation (corresponding to the PVP layer thickness), an isotropic dipole orientation⁴⁴, an SNP diameter of 100 nm, a CNP side length of 100 nm, and PDMS medium. For CNP, the edges

and corners of silver CNP were rounded by 3 nm and 5 nm, respectively, according to the previous microscope image studies³⁸. By varying the shape of the Ag NPs, an effect on emitter decay rates was analyzed (Figs. 3a and b). Our simulations further suggest that embedding single CNPs with single CsPbBr₃ NCs in a PDMS matrix can enhance the LDOS by up to 98 times, particularly near the CNP edges or corners comparing to SNP. The full equations for this analysis are provided in the Supporting Information.

Following an initial assessment of single-emitter interactions, the analysis was extended to systems with multiple emitters in single Ag NPs. Using Monte Carlo simulations, 100,000 configurations were generated with random emitter distributions based on the estimated surface coverage in the real samples: 68 and 126 emitters for SNPs and CNPs, respectively (see Methods). Due to the substantial number of configurations, nonlocal optical responses⁴⁵ were not included in our calculations, as these effects are statistically averaged out when using the ratio definitions in Eq. 1. A histogram analysis of LDOS enhancement across all configurations indicates that CNPs yield a greater enhancement than SNPs (Figs. 3c and d). Specifically, SNPs achieve an average enhancement factor of (6.84 ± 0.01) , whereas CNPs reach (14.60 ± 2.60) . The smaller variation in SNPs reflects their spheroid shape and absence of sharp edges, which are present in CNPs. However, those values should be corrected with the QE of CsPbBr₃ NC and C_{coup} of our multiple NC-NP systems.

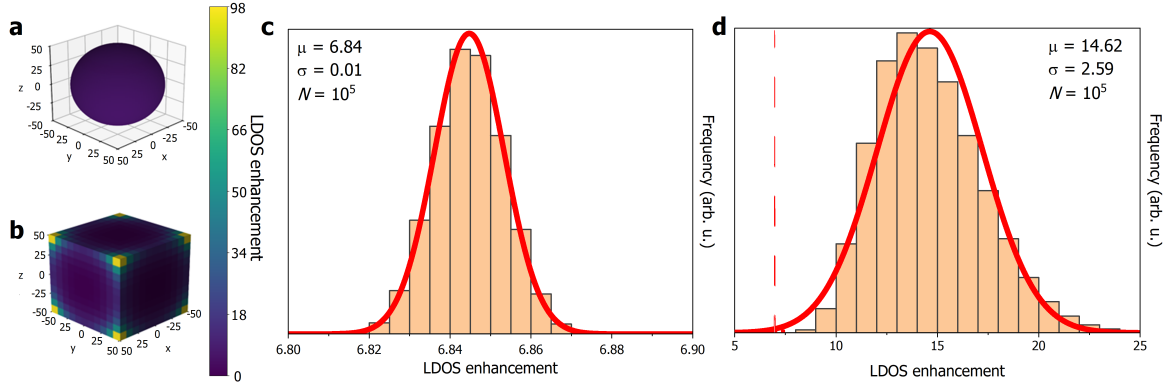


FIG. 3. **Theoretical calculations.** **a, b** Three-dimensional maps of local density of states (LDOS) enhancements for CsPbBr₃ NCs doped with SNPs (**a**) and CNPs (**b**), respectively. **c, d** The histograms of LDOS enhancements for SNPs- (**c**) and CNPs-doped (**d**) samples. Red dashed line in **d** represents the normal distribution from **c**, to show the overlap with the distribution tail. The histograms represent 10,000 different random configurations of 68 and 126 emitters for SNPs and CNPs, respectively.

Experiments to probe the Purcell enhancements were then performed and analyzed for two sample points each. Optical characterizations were initially carried out through PL and TRPL measurements. Before determining the Purcell enhancements from both measurements, it was necessary to measure the CsPbBr₃ NC *QE* using an integrating sphere. From the series of measurements, the average *QE* value was found to be $(55 \pm 15)\%$ (Supporting Fig. S4). With this *QE*, it is expected to see moderate enhancements of integrated luminescence intensities and decay rates^{11,25}. Fig. 4a displays the RT PL spectra, where samples doped with Ag NPs exhibit significantly enhanced intensities compared to pure CsPbBr₃ samples. Specifically, the integrated PL intensity enhancements of for SNPs ($P_{\text{PL}}^{\text{SNP}}/P_{\text{PL}}^{\text{o}}$) and CNPs ($P_{\text{PL}}^{\text{CNP}}/P_{\text{PL}}^{\text{o}}$) are (3.20 ± 0.20) and (4.10 ± 0.20) fold, respectively. Fig. 4b presents the RT TRPL decay curves, with both Ag-doped samples showing faster PL decays. At first sight, there are two decay components related to the multiexciton generations in CsPbBr₃ NCs^{8,46}. Using bi-exponential decay fitting (Supporting Table S1), the shortest decay time constants decrease from (0.99 ± 0.03) ns in pure CsPbBr₃ to (0.71 ± 0.05) ns and (0.61 ± 0.04) ns in SNPs- and CNPs-doped samples, respectively. Both values are still slower than

0.3 ns of instrument response function (IRF), see Methods. The average PL decay times ($\bar{\tau}_{\text{PL}}$) at RT are (4.02 ± 0.13) ns, (1.61 ± 0.08) ns, and (0.94 ± 0.06) ns for pure, SNPs-, and CNPs-doped samples, respectively, resulting in PL decay rate enhancements of (2.48 ± 0.17) and (4.20 ± 0.31) fold for SNPs- ($\Gamma_{\text{PL}}^{\text{SNP}}/P_{\text{PL}}^o$) and CNPs-doped samples ($\Gamma_{\text{PL}}^{\text{CNP}}/P_{\text{PL}}^o$), respectively.

Subsequent to the PL and TRPL measurements, XL and TRXL characterizations were performed, anticipating similar enhancements in integrated luminescence and decay rate¹¹. As shown in Fig. 4c, XL spectra reveal enhancements of (1.71 ± 0.09) and (1.92 ± 0.13) fold for SNPs- ($P_{\text{XL}}^{\text{SNP}}/P_{\text{XL}}^o$) and CNPs- ($P_{\text{XL}}^{\text{CNP}}/P_{\text{XL}}^o$) doped samples, respectively. Room-temperature TRXL decay curves (Fig. 4d) reveal a tri-exponential decay with a notable long (> 10 ns) component, detailed in Supporting Table S1. The additional component appears in TRXL decay curves due to higher energy excitation of TRXL than that of TRPL generating multiple intermediate states, including trap-defect states, and involves multi-excitonic processes^{8,46}. The fastest decay time is still that of CNPs with (0.67 ± 0.04) ns and this is still slower than IRF, see Methods. The average decay times $\bar{\tau}_{\text{XL}}$ decrease from (7.55 ± 0.12) ns in the pure sample to (4.18 ± 0.13) ns and (3.70 ± 0.10) ns in the respective SNPs- and CNPs-doped samples, yielding XL decay rate enhancements, $\Gamma_{\text{XL}}^{\text{SNP}}/P_{\text{XL}}^o$ and $\Gamma_{\text{XL}}^{\text{CNP}}/P_{\text{XL}}^o$, of (1.84 ± 0.07) and (2.08 ± 0.06) fold, respectively. These enhancements correlate with surface plasmon resonance effects, which increase the LDOS near the NPs, favoring higher radiative recombination probabilities. CNPs demonstrated the strongest enhancements, likely due to their intense and narrow scattering spectra, optimizing overlap with the CsPbBr₃ NC emission spectrum (Supporting Fig. S2). Given the enhancements in both light yield and decay rates, future investigations will focus on coincidence measurements, as CNP doping could reduce the overall coincidence time resolution ($\text{CTR} \propto \sqrt{\tau/\text{LY}}$) by 50% compared to pure CsPbBr₃, which is crucial for PET applications⁴⁶.

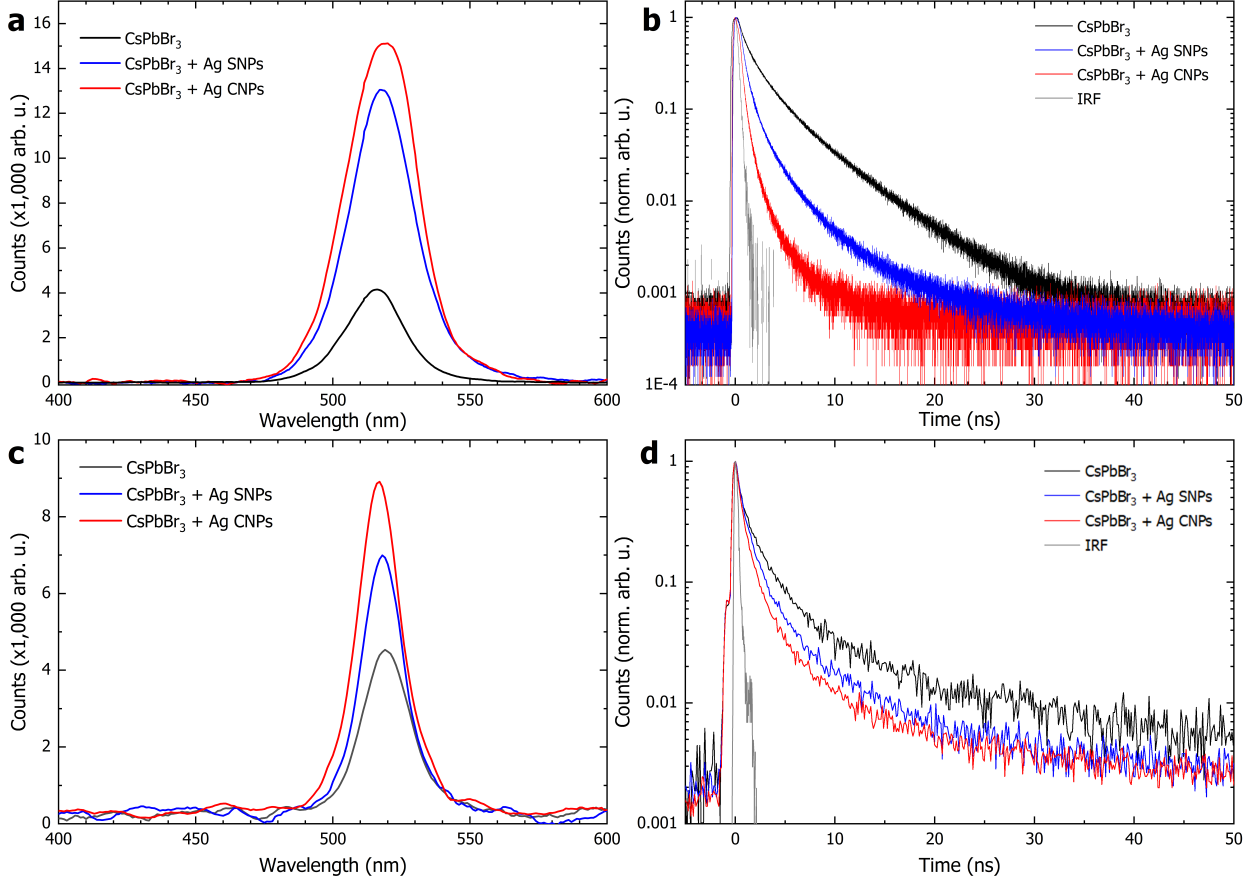


FIG. 4. **Optical and X-ray excitation characterizations.** **a, b** The photoluminescence (PL) spectra (**a**) and time-resolved PL decay curves (**b**). **c, d** The X-ray luminescence (XL) spectra (**c**) and time-resolved XL decay curves (**d**). All measurements were performed at room temperature (RT). Notably, the PL spectrum and the decay curve for $\text{CsPbBr}_3 + \text{CNPs}$ exhibits the most significant plasmonic enhancement, reaching about 4 fold, while other enhancements demonstrate approximately between 2- and 3-fold enhancements.

To evaluate potential enhancements in QE at low temperatures (LT), we conducted temperature-dependent PL and XL measurements (Supporting Fig. S5). For pure samples, there is a very small redshift in XL spectra at 10 K of about 3 nm due to exciton-phonon interaction in CsPbBr_3 NCs⁴⁶. Remarkably, for CNPs-doped samples, a much larger 10-nm redshift in emission peak wavelength is observed at LT, with the XL peak shifting from 518 nm at RT to 528 nm at 10 K, bringing it closer to the 541-nm peak of the CNP scattering spectrum (Supporting Fig. S2). The large shift in CNPs strongly suggests an enhanced light-matter coupling between CsPbBr_3 NC Ag CNPs emissions^{38,39}. Additionally, both PL

and XL intensities increase at LT following the same quenching behavior (see Supporting Tables S2 and S3 for parameters) and indicating a reduced contribution from non-radiative recombination processes. This directly implies a boosted QE and, consequently, elevated Purcell enhancements, see Supporting Information²⁶. For example, at 80 K, the integrated PL intensity ratios $P_{\text{PL}}^{\text{SNP}}/P_{\text{PL}}^{\circ}$ and $P_{\text{PL}}^{\text{CNP}}/P_{\text{PL}}^{\circ}$ increase to (5.74 ± 0.34) and (6.52 ± 0.41) , respectively. This QE increase at lower temperatures is also supported by the absence of traps in thermoluminescence (TL) measurements (Supporting Fig. S6), which is advantageous for scintillator applications that are fast and accurate in ionizing radiation detection¹. Furthermore, the absence of afterglow at 10 K explains why the enhancements under X-ray excitation are clearly observed.

Building on the observed improvements, X-ray imaging (Figs. 5a-c) reveals that Ag NP-doped samples demonstrate enhanced brightness, with maximum intensity measurements reaching 1,000 counts for pure CsPbBr₃, 1,950 counts for SNPs-doped, and 2,250 counts for CNPs-doped materials. This results in notably clearer imaging than previously reported in plasmonic scintillator¹¹. Detailed cross-sectional images and resolution card imaging are presented in Supporting Fig. S7 and Supporting Table S4. The best spatial resolution is 5 line pairs per millimeter at 0.2 modulation transfer function, similar to that observed by Maddalena et al.⁴⁶. However, this study focuses on the Purcell enhancements in X-ray imaging intensities, where $P_{\text{Img}}^{\text{SNP}}/P_{\text{Img}}^{\circ}$ and $P_{\text{Img}}^{\text{CNP}}/P_{\text{Img}}^{\circ}$ reach enhancements of (1.95 ± 0.10) and (2.25 ± 0.10) fold, respectively. Additionally, such NC-NP configuration may also facilitate directed emission in CNP-doped materials, which can be aligned during fabrication⁴⁷.

From all measurements, they consistently show the highest enhancements in samples doped with CNPs (Fig. 5d). Pulse height measurements were also conducted using 59.5 keV γ -rays from ²⁴¹Am. However, the photopeaks remain inconspicuous due to the insufficient thickness or low concentration compared to the absorption length (Supporting Fig. S2). The extended tail observed in the pulse height spectrum of CNP-doped materials may suggest enhancement (Supporting Fig. S8). The values of FDTD simulations with single Ag NP approach were corrected with QE and C_{coup} resulting with (2.63 ± 0.79) and (5.62 ± 1.71) fold for CsPbBr₃ NCs inside ensembles of Ag SNPs and CNPs, respectively. Thus, we found that experimental enhancements from PL and TRPL become similar to the theoretical values, within error margin (Fig. 5d and Supporting Information). Smaller absolute enhancements observed under X-ray characterization compared to those observed under optical excitation

can be attributed to several factors especially nonproportionality between PL and XL^{46,48,49}. In CsPbBr₃ NCs^{46,48}, such nonproportionality with different low-energy excitations is very significant in comparison to two-dimensional perovskite materials^{11,50}. Moreover in PL, the yield is directly influenced by quenching and the radiative probability, making the impact of Purcell enhancement straightforward. In contrast, scintillation involves multiple intermediate stages before reaching the final stage of light emission. Consequently, the yield is determined by various quenching phenomena occurring throughout these stages. The Purcell effect, however, acts solely on the final stage, resulting in a reduced overall influence on the entire scintillation process.

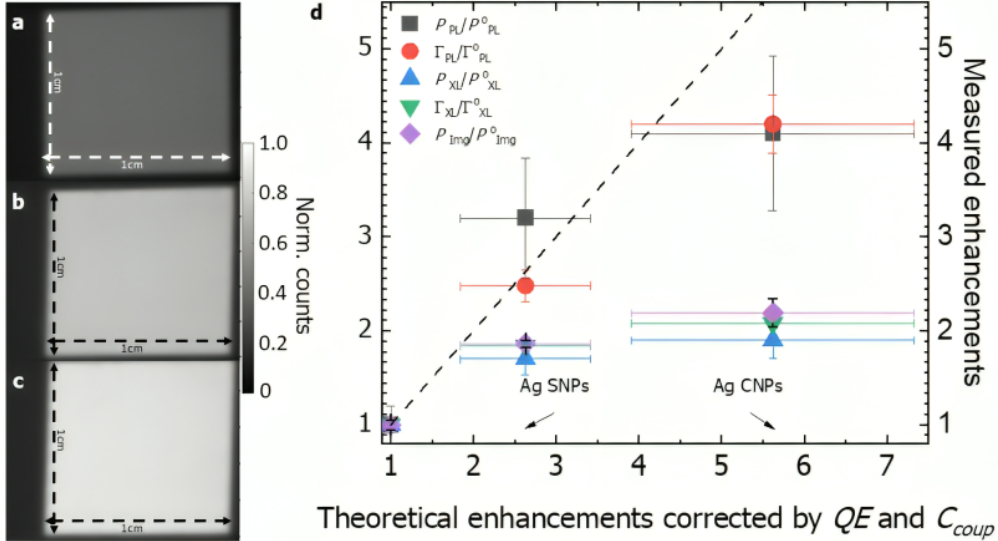


FIG. 5. **X-ray images and Purcell enhancements.** **a, b, c**, X-ray images of a card featuring a square hole with a side length of 1 cm for pure CsPbBr₃ (**a**), CsPbBr₃ + SNPs (**b**), and CsPbBr₃ + CNPs (**c**). **d**, The measured (at RT) vs theoretical LDOS enhancements, derived from FDTD calculations with correction factors: assumptions of (55 ± 15) % quantum (*QE*) and (70 ± 8) % NC-NP coupling (*C_{coupl}*) efficiencies. The measured enhancements for integrated PL intensities, PL decay rates, integrated XL intensities, XL decay rates, and X-ray image intensities are represented as $P_{\text{PL}}/P_{\text{PL}}^{\text{o}}$, $\Gamma_{\text{PL}}/\Gamma_{\text{PL}}^{\text{o}}$, $P_{\text{XL}}/P_{\text{XL}}^{\text{o}}$, $\Gamma_{\text{XL}}/\Gamma_{\text{XL}}^{\text{o}}$, and $P_{\text{Img}}/P_{\text{Img}}^{\text{o}}$, respectively. Black dashed line shows one-to-one match.

III. DISCUSSION

This study demonstrates the first practical application of the Purcell effect to enhance X-ray scintillation in CsPbBr₃ NCs embedded in a millimeter-thick PDMS matrix. By introducing Ag SNPs and Ag CNPs, significant improvements in PL, XL, TRPL, and TRXL were observed, with the most pronounced enhancements achieved in samples doped with Ag CNPs. At RT, these samples exhibited up to (3.20 ± 0.20) - and (4.20 ± 0.31) -fold enhancements in CsPbBr₃ NCs with Ag SNPs and Ag CNPs, respectively. Given that the light yield of CsPbBr₃ NCs is 21 ph/keV^{8,46,51}, these Purcell-enhanced scintillators could exhibit significantly higher light yields (ranging from 43 to 86 ph/keV), ultrafast decay times (ranging from 0.61 to 0.67 ns), and zero afterglow, making them ideal for advanced medical imaging (e.g., PET and PCCT) and security applications³⁷. Our work shows an alternative strategy to overcome the thin film limitations^{11–15} and achieves stable enhancements that are two to four times larger than those reported for nanoparticle-doped liquid scintillators⁵². Furthermore, our millimeter-scale approach, based on a scalable self-assembly process, supports the emerging need for large, high-performance nanophotonic scintillators¹⁰, circumventing typical thickness limitations. Future research will focus on optimizing nanoemitters for improved QE , utilizing core-shell structures to minimize non-radiative losses, exploring nanoplatelet configurations for optimal dipole alignment, and increasing Stokes shifts to reduce self-absorption⁵¹. This work establishes Purcell-enhanced scintillators as promising tools for next-generation imaging and real-time radioactive gas detection^{53,54}.

IV. METHODS

FDTD calculations. Simulations were conducted using Lumerical FDTD Solutions. A simulation region span of 400 nm was used across all axes with Perfectly Matched Layer (PML) boundary conditions, a mesh size of 0.5 nm, and at 300 K. The Ag NPs used the permittivity from⁵⁵, with the respective 3- and 5-nm rounded edges and corners for the CNPs. To represent the emitters in the calculations, a single broadband dipole source was placed at the emitter position^{56,57} (i.e., 5 nm above the NP surface), oriented parallel or perpendicular to the NP surface. Simulations were run for each of these single dipoles at different positions along the Ag nanoparticle surface. The Purcell factor in each emitter position was calculated

as the ratio of the emitted power with and without the Ag nanoparticles and was averaged from the parallel and perpendicular orientations, assuming an isotropic emission⁴⁴.

CsPbBr₃ NCs synthesis. NCs were prepared by a hot injection method as described in detail by Ghorai and others⁵⁸. The only difference was the choice of toluene as a protective medium instead of hexane for NCs solution. The side lengths from the TEM of the single CsPbBr₃ NC are (7.30 ± 0.20) nm and (6.76 ± 0.20) nm, see Figure 2.

Sample preparation. Three solutions were prepared, each containing a 20-weight percent concentration of CsPbBr₃ NCs. One solution was left unchanged, while the other two were supplemented with Nanocompsix Ag SNPs and Ag CNPs, respectively, at a 1:1 weight ratio of Ag to NCs. These solutions were carefully processed to promote NC attachment to the NP^{38,39}. A polymer matrix was prepared by mixing 2.7 grams of Sylgard 184 Silicone Elastomer (PDMS) with 0.3 grams of curing agent. Each NC solution was then added to the polymer, and the mixture was agitated on a vortex mixer for 5 minutes to ensure even distribution of CsPbBr₃ NCs and Ag NPs. The mixture was divided equally into three vials and cured in a vacuum oven at 120°C for 24 hours. After curing, the samples were removed from the mold, resulting in smooth surfaces with slightly rough edges, as illustrated in Fig. 1a. Each sample measured 1.5 cm in diameter and 0.5 cm in thickness.

PL and TRPL measurements. The initial phase of our experimental procedures aimed at assessing PL involved employing a picosecond laser diode operating continuously at a wavelength of 375 nm to stimulate the samples. Precise excitation focusing and simultaneous signal acquisition were facilitated by an objective microscope. Following this, the collected PL signal was meticulously filtered using a 405 nm upper pass filter and acquired it using a high-sensitivity visible light spectrometer with optical fiber. Transitioning to TRPL measurements, an adjustment of the operation mode of the laser diode was done, switching from continuous wave (CW) mode to pulse operation with a 10 MHz repetition rate. The emitted PL signal, filtered with a specific long-pass filter with a cut-on wavelength of 405 nm, was directed towards a single-photon avalanche photodiode. The temporal behavior of this signal was thoroughly scrutinized using time-correlated single-photon counting electronics with an IRF of 0.3 ns¹¹. For temperature-dependent PL and TRPL measurements, a Linkam HFS600E-PB4 cryostat with a liquid nitrogen cooling system was employed. This setup enabled us to conduct measurements ranging from 80K to 370K with increments of 10K.

XL and TL. Experimental methodology entailed a comprehensive setup meticulously designed to accommodate both XL and TL assessments. This integrated configuration incorporated essential components, including an Inel XRG3500 X-ray generator operating at 45 kV / 10 mA with a copper anode tube, an Acton Research Corp. SpectraPro-500i monochromator, a Hamamatsu R928 photomultiplier tube (PMT), and an APD Cryogenic Inc. closed-cycle helium cooler. After reducing the temperature to 10 K, the crystals were exposed to X-rays for 10 minutes. Subsequently, TL glow curves were captured, employing a gradual heating rate of 0.14 K/s across a temperature range spanning from 10 to 350 K. Following this, XL spectra were acquired at discrete temperatures, commencing from 350 K and descending in 10 K increments down to 10 K. This systematic sequence of measurements was deliberately chosen to mitigate potential influences arising from the thermal release of charge carriers, ensuring a comprehensive assessment of the emission output.

Time-resolved XL. Time-correlated single photon counting method was utilized to obtain RT time-resolved X-ray decay curve measurement with a Start:Stop ratio of approximately 5000:1. X-ray pulses were generated using a PicoQuant LDHP-C-440M pulsed diode laser, derived from a Hamamatsu N5084 X-ray tube stimulated by light, with a high voltage set to 35 keV. Laser activation was facilitated by a PicoQuant laser driver, with its reference output serving as the start signal, synchronized with an Ortec 567 time-to-amplitude converter (TAC). To ensure precision in timing, An Ortec 462 time calibrator was employed to calibrate the bin width. The emitted photons were captured and analyzed using a digital PicoQuant analyzer. The total IRF of the system is similar to TRPL of 0.3 ns¹¹. Sample positioning took place within a closed-cycle helium cryostat operating under pressures below 10⁻⁴ mbar, maintaining optimal experimental conditions.

X-ray imaging. In the X-ray imaging setup, 500- μ m-thick perovskite films on glass, see Supporting Fig. S9, were positioned in front of an LD Didactic 554 800 X-ray apparatus with a Mo-source operating at 17.5 keV, 1 mA current, and 35 keV voltage. A Type-18A line pattern card, with a lead thickness of 125 mm, was placed between the X-ray source and the film to minimize light scattering by positioning the pattern and the film as close as possible. The samples need to be thinner than those in Figs. 1f and 1g for best resolution performance⁴⁶. To capture the film's scintillation, an Allied Vision Mako U 130B camera with a 1.4-second exposure time and a conversion lens of 8-mm focal length was used. Image analysis involved calculating the edge spread function and its first derivative, the line spread

function. The modulation transfer function was then determined by computing the modulus of the Fourier transform of the line spread function.

ACKNOWLEDGMENTS

All authors acknowledge research funds from the National Science Center, Poland under grant OPUS-24 no. 2022/47/B/ST5/01966. **F.M. and C.D.** acknowledge the financial support from the Ministry of Education, Singapore, under its AcRF Tier 2 grant (MOE-T2EP50121-0012). **F.A.A.N.** acknowledges funding by the Indonesian Endowment Fund for Education (LPDP) on behalf of the Indonesia Ministry of Education, Culture, Research and Technology, which is managed by Universitas Indonesia under INSPIRASI Program (Grant No PRJ-61/LPDP/2022 and 612/E1/KS.06.02/2022). **F.A.A.N.** also acknowledges Wildan P. Tresna for his help in the initial phase of the FDTD calculations. **S.M.** acknowledges the support by the European Commission and the Polish National Science Centre under the Marie Skłodowska-Curie COFUND grant (POLONEZ BIS 2) under Agreement No: UMO-2022/45/P/ST3/04170. **W.D.** acknowledges Mohanad Eid for his assistance in the radio- and thermoluminescence measurements. **M.M.** acknowledges his on-leave status from Nicolaus Copernicus University in Torun, Torun 87-100, Poland.

V. AUTHOR CONTRIBUTIONS STATEMENT

M.M.: Methodology, Formal analysis, Investigation, Conceptualization, Writing-original draft, Writing-review & editing, **W.Y., D.K., F.M., S.M., Y.T.A., W.Z., M.E.W, K.J.D, N., C.D.,J.C.:** Formal analysis, Investigation, Writing-review & editing; **W.D., F.A.A.N., L.J.W.** Supervision, Resources, Writing-review; **M.D.B.** Conceptualization, Supervision, Resources, Writing-review & editing, Project administration, Funding acquisition.

VI. ADDITIONAL INFORMATION

Supporting Information Supporting Information is available free of charge on the **Competing interests** The authors declare no competing interests.

VII. SUPPORTING INFORMATION

LIGHT-MATTER INTERACTIONS IN NANOPLASMONIC SCINTILLATION

High-energy particles, particularly X-rays, interact with scintillators, converting their energy into visible light. High-energy electrons generated by these particles lose energy through excitation, forming multiple secondary electrons and holes within the scintillation material, each with unique spatial positions and orientations. These electrons and holes subsequently form electron-hole pairs or dipole emitters. These pairs then undergo relaxation, either radiatively, emitting visible photons, or non-radiatively, dissipating energy as heat.

In the case of a bare scintillator, the emission characteristics, such as emission rate, emission power, and emission direction, are solely determined by the intrinsic properties of the scintillation material, including its atomic structure. The dipole emission primarily couples into the radiative mode with an emission rate of Γ_{bare} , representing the number of photons produced by the dipole emitter. The photon flux arriving at the photodetector is given by Γ_{bare} multiplied by the energy transmission coefficient T_{bare} , which quantifies the efficiency of visible photon transmission from the dipole emitter to the detector. Thus, the emission power (or visible photon flux) is proportional to the emission rate and energy transmission coefficient:

$$\frac{dN_{\text{bare}}}{dt} = \Gamma_{\text{bare}} T_{\text{bare}} = \frac{P_{\text{bare}}}{\hbar\bar{\omega}} \quad (\text{S4})$$

where N , t , P , and $\hbar\bar{\omega}$ represent the detected photon number, time, detected emission power, and average optical photon energy, respectively. Then, with the introduction of a nanophotonic design, especially a nanoplasmonic structure (as studied here), the scenario changes significantly. Nanoplasmonic designs, particularly those with structures on length scales comparable to visible wavelengths, enhance emission properties in two ways. First, they modify the intrinsic emission rate of dipole emitters within scintillators through the well-known Purcell effect, represented as $\Gamma = Fp\Gamma_{\text{bare}}$, where Fp is the Purcell factor. The Purcell factor quantifies the enhancement of the spontaneous emission rate of a quantum emitter, such as CsPbBr₃ NC in our case, in the presence of electromagnetic modes. This enhancement is directly proportional to the local density of states (LDOS) at the emitter's

position, i.e., $Fp \propto \text{LDOS}$. The local density of states can be calculated as:

$$\text{LDOS}(\mathbf{r}, \omega) = \frac{6\omega}{\pi c^2} [\mathbf{n}_\mu \cdot \text{Im} \{ \mathbb{G}(\mathbf{r}, \mathbf{r}, \omega) \} \cdot \mathbf{n}_\mu] \quad (\text{S5})$$

where \mathbf{r} is the location of the dipole, μ is the dipole moment, c is the speed of light in a vacuum, and $\mathbb{G}(\mathbf{r}, \mathbf{r}', \omega)$ is the Green's function at the dipole's location.

Second, the nanoplasmonic structure influences the transmission coefficient T for internal photons, modulating how they enter the external environment for photodetector capture. This transmission coefficient is given by $T = \eta T_{\text{bare}}$. The detected photon flux in the presence of a nanophotonic design is thus:

$$\frac{dN}{dt} = \Gamma T = \eta Fp \Gamma_{\text{bare}} T_{\text{bare}} = \frac{P}{\hbar\omega} \quad (\text{S6})$$

As a result, the photodetector photon flux is enhanced by a factor of ηFp . This work explores the Purcell factor, Fp , for a dipole emitter near both spheroid and cuboid nanoparticles (NPs). For the further derivations of Fp , we initially presume quantum efficiency (QE) is unity but the effect of the QE to Fp will be explained later.

Purcell Factor for a Dipole near a spheroid NP

For a single spheroid NP, the Purcell factor for a dipole close to the NP^{35,36} includes two components based on dipole polarization. The perpendicular component, $Fp_{\perp}^{\text{sphere}}$, is given by:

$$Fp_{\perp}^{\text{sphere}} = \frac{3}{2} \sum_{n=1}^{\infty} n(n+1)(2n+1) \left| \frac{j_n(y_{\text{med}}) + b_n h_n^{(1)}(y_{\text{med}})}{y_{\text{med}}^2} \right|^2 \quad (\text{S7})$$

Similarly, the parallel component, $Fp_{\parallel}^{\text{sphere}}$, is expressed as:

$$Fp_{\parallel}^{\text{sphere}} = \frac{3}{4} \sum_{n=1}^{\infty} (2n+1) \left\{ \left| j_n(y_{\text{med}}) + a_n h_n^{(1)}(y_{\text{med}}) \right|^2 + \frac{\left| [y_{\text{med}} j_n(y_{\text{med}})]' + b_n [y_{\text{med}} h_n^{(1)}(y_{\text{med}})]' \right|^2}{y_{\text{med}}^2} \right\} \quad (\text{S8})$$

Here, $y_{\text{med}} = k_{\text{med}} r'$, where $k_{\text{med}} = k_0 n_2$, and $k_0 = \omega/c$. r , r' , ω , c , \perp , and \parallel denote the position of the electric field, the dipole emitter position (a CsPbBr₃ NC) within a medium (PDMS) at approximately 5 nm from the NP, the emission angular frequency, the speed of

light, radial dipoles, and tangential dipoles, respectively. j_n and $h_n^{(1)}$ are spherical Bessel functions.

Since Fp is linked to maximum enhancement, we define $Fp^{sphere} = Fp_{\perp}^{sphere}$ for a dipole emitter with perpendicular orientation to the surface. In the isotropic case, the Purcell factor becomes $Fp^{sphere} = Fp_{iso}^{sphere} = \frac{1}{3}Fp_{\perp}^{sphere} + \frac{2}{3}Fp_{\parallel}^{sphere}$.

Purcell factor for a dipole near a cuboid NP

To approximate the Purcell factor for a dipole near a cuboid NP, we can utilize findings from prior studies^{59,60}. However, these previous solutions primarily focus on configurations involving a substrate. Another possible approach considers plasmon resonances as an eigenvalue problem⁶¹, allowing us to approximate the Purcell factor for a cuboid NP via radiation corrections to electrostatic models. However, this method is valid only when the incident radiation wavelength is significantly larger than the NP dimensions.

In our approach, we return to a simpler approximation, analyzing the case where the dipole is near a cuboid NP surface, positioned away from edges and corners. For a dipole orientation parallel to the surface, the Purcell factor is given by

$$Fp_{\parallel}^{cube}(d, \omega) = 1 + \frac{3}{4k_0} \text{Re} \left\{ \int_0^{\infty} dk_s \left[\frac{k_s}{k_{\perp}} \left(R^{TM} - \frac{k_{\perp}^2}{k_0^2} R^{TE} \right) e^{2ik_{\perp}d} \right] \right\}, \quad (\text{S9})$$

where $k_0 = \omega/c$, k_s is the in-plane wavenumber, k_{\perp} is the normal wavenumber, and R^{TM} and R^{TE} are the Fresnel reflection coefficients for TM and TE polarized light, respectively. Here, ω is the emission angular frequency, c is the speed of light, and d is the distance between the dipole and the surface. The Fresnel reflection coefficients can be expressed as

$$R^{TE} = \frac{k_{0,z} - k_{metal,z}}{k_{0,z} + k_{metal,z}}, \quad R^{TM} = \frac{k_{0,z}\epsilon_{metal,y} - k_{metal,z}}{k_{0,z}\epsilon_{metal,y} + k_{metal,z}}, \quad (\text{S10})$$

where

$$k_{0,z} = \sqrt{k_0^2 - k_s^2}, \quad k_{metal,z} = \sqrt{k_0^2\epsilon_{metal,r} - k_s^2}, \quad (\text{S11})$$

and $\epsilon_{metal,r}$ is the relative permittivity of the metal. For a dipole orientation perpendicular to the surface, the Purcell factor becomes

$$Fp_{\perp}^{cube}(d, \omega) = 1 + \frac{3}{2k_0} \text{Re} \left\{ \int_0^{\infty} dk_s \left[\frac{k_s^3}{k_{\perp}k_0^2} R^{TE} e^{2ik_{\perp}d} \right] \right\}. \quad (\text{S12})$$

For an isotropic case, the Purcell factor Fp^{cube} is given by $Fp_{iso}^{cube} = \frac{1}{3}Fp_{\perp}^{cube} + \frac{2}{3}Fp_{\parallel}^{cube}$.

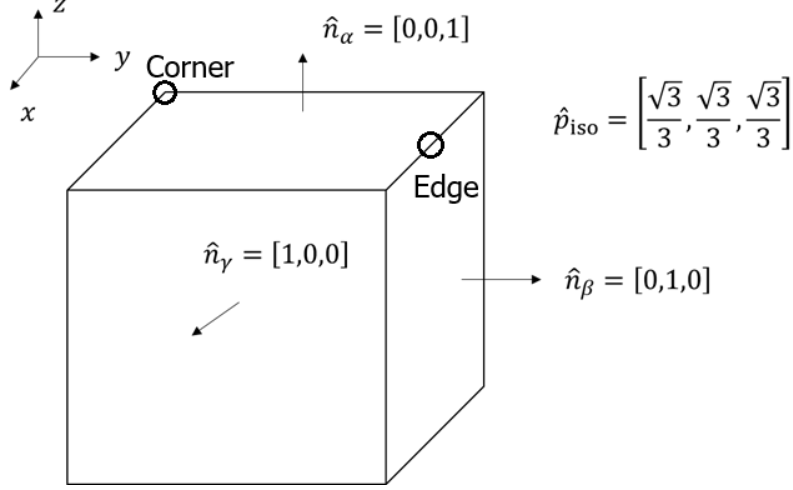


FIG. S1. **Representations of dipole orientation in the isotropic case.** Dipole orientations with their cuboid NP surfaces. The circular areas define the edge and the corner.

If the dipole is placed near the edge of a nanoplasmonic cube, the interaction with multiple surfaces alters the effective orientation. Here, we define the normal vectors of metal surfaces 1 and 2 as \hat{n}_1 and \hat{n}_2 , respectively, with the dipole orientation unit vector \hat{p} . The distances from the dipole to surfaces 1 and 2 are d_1 and d_2 , respectively. The isotropic Purcell factor $Fp^{cube,edge}$ for this configuration can be approximated by

$$Fp^{cube,edge}(\mathbf{r}, \omega, \hat{p}) = 1 + \{ [Fp_{\parallel}^{cube}(d_1, \omega) - 1] |\hat{p} \times \hat{n}_1|^2 + [Fp_{\parallel}^{cube}(d_2, \omega) - 1] |\hat{p} \times \hat{n}_2|^2 + [Fp_{\perp}^{cube}(d_1, \omega) - 1] |\hat{p} \cdot \hat{n}_1|^2 + [Fp_{\perp}^{cube}(d_2, \omega) - 1] |\hat{p} \cdot \hat{n}_2|^2 \}. \quad (S13)$$

For dipoles with isotropic orientations, we can use $\hat{p}_{iso} = [\sqrt{3}/3, \sqrt{3}/3, \sqrt{3}/3]$, $\hat{n}_\alpha = [0, 0, 1]$, $\hat{n}_\beta = [0, 1, 0]$, and $\hat{n}_\gamma = [1, 0, 0]$ for Eq. S13 by noting that surfaces 1 and 2 are two of the surfaces (α, β, γ), depending on the dipole position, see Supporting Fig. S1. The definition for the isotropic Purcell factor then becomes $Fp_{iso}^{cube,edge}(\mathbf{r}, \omega) = Fp^{cube,edge}(\mathbf{r}, \omega, \hat{p}_{iso})$.

For a dipole placed in the corner of a nanoplasmonic cube, we extend the edge-based approach to include interactions with three surfaces. Here, the normal vectors of surfaces 1, 2, and 3 are \hat{n}_1 , \hat{n}_2 , and \hat{n}_3 , respectively, and the distances from the dipole to these surfaces are d_1 , d_2 , and d_3 . The isotropic Purcell factor $Fp^{cube,corner}$ is given by

$$Fp^{cube,corner}(\mathbf{r}, \omega, \hat{p}) = 1 + \{ [Fp_{\parallel}^{cube}(d_1, \omega) - 1] |\hat{p} \times \hat{n}_1|^2 + [Fp_{\parallel}^{cube}(d_2, \omega) - 1] |\hat{p} \times \hat{n}_2|^2 + [Fp_{\parallel}^{cube}(d_3, \omega) - 1] |\hat{p} \times \hat{n}_3|^2 + [Fp_{\perp}^{cube}(d_1, \omega) - 1] |\hat{p} \cdot \hat{n}_1|^2 + [Fp_{\perp}^{cube}(d_2, \omega) - 1] |\hat{p} \cdot \hat{n}_2|^2 + [Fp_{\perp}^{cube}(d_3, \omega) - 1] |\hat{p} \cdot \hat{n}_3|^2 \}. \quad (S14)$$

For the dipoles at the corner. using the same analogy with the dipoles at the edge, we can use $\hat{p}_{iso} = [\sqrt{3}/3, \sqrt{3}/3, \sqrt{3}/3]$, $\hat{n}_1 = [0.0, 1]$, $\hat{n}_2 = [0.1, 0]$, and $\hat{n}_3 = [1.0, 0]$. For the Purcell factor, $Fp_{iso}^{cube,corner}(\mathbf{r}, \omega) = Fp^{cube,corner}(\mathbf{r}, \omega, \hat{p}_{iso})$.

ABSORPTION LENGTH AND SCATTERING SPECTRA

A reduction of absorption length is noticeable in Fig. S2b. Three relevant X-ray energies of 10, 45, and 662 keV were selected for evaluation. Absorption lengths were reduced as follows $0.18 \rightarrow 0.03$ mm, $2.68 \rightarrow 0.34$ mm, and $70.32 \rightarrow 36.35$ mm for 10, 45, and 66 keV, respectively.

For the scattering spectra, the measurements of individual Ag NPs were carried out in home-built microscope settings with a xenon light source (Thorlabs) focused through a $100\times$ objective lens (NA = 0.95) in dark-field geometry³⁸. The scattered light was then collected by the same lens and directed into the hyperspectral system (Cytoviva) for spectral measurement of the individual particles.

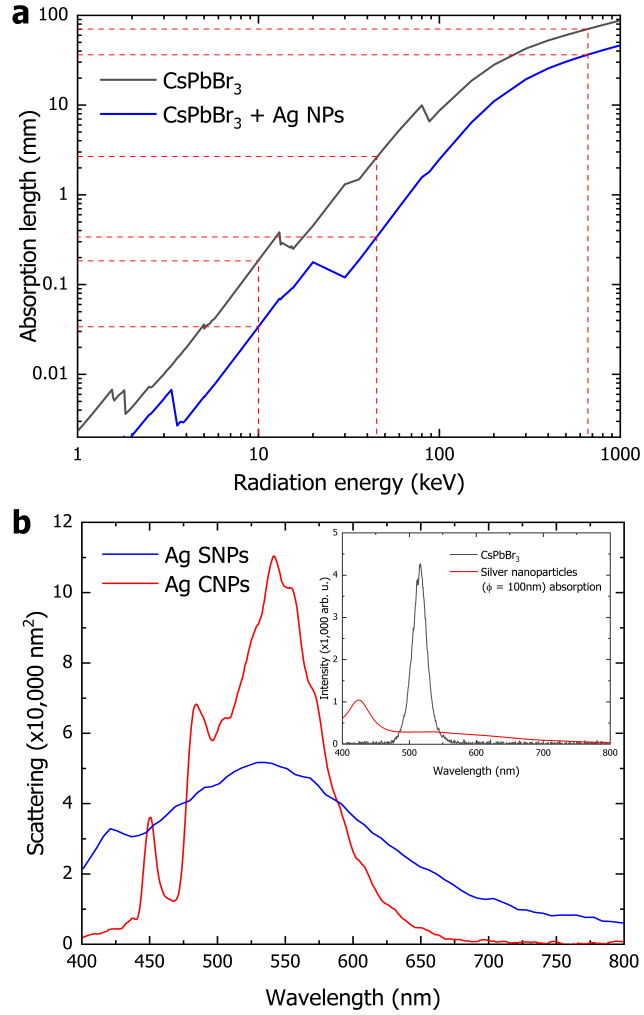


FIG. S2. **Theoretical absorption length and the additional optical characterisations of the samples.** **a**, Absorption length of CsPbBr₃ NCs in PDMS (black line), and Ag NPs-doped sample (blue line). The dashed lines present the critical absorption lengths for 10, 50, and 662 keV, respectively. **b**, The scattering spectra of Ag SNPs and Ag CNPs compared. Inset presents PL spectra of pure CsPbBr₃ NCs in PDMS (black line) and absorption spectra of Ag NPs with a diameter of 100nm (red curve).

FDTD CALCULATIONS

Absolute decay rates, such as Γ_{rad} , $\Gamma_{\text{rad}}^{\circ}$, Γ_{nrad} , cannot be calculated with FDTD. However, the quantum mechanical decay rate in an inhomogeneous environment Γ_{dip} and the

classical power radiated by the dipole in the same environment P_{dip} are related by:

$$\frac{\Gamma_{\text{dip}}}{\Gamma_{\text{rad}}^o} = \frac{P_{\text{dip}}}{P_{\text{rad}}^o} \quad (\text{S15})$$

Where Γ_{rad}^o and P_{rad}^o are the decay rate and radiated power of the dipole in a homogeneous environment.

The Purcell factor is the emission rate enhancement shown as

$$F_p = \frac{\Gamma_{\text{dip}}}{\Gamma_{\text{rad}}^o} \quad (\text{S16})$$

Therefore, the Purcell factor can be calculated using a simple built-in source-power function in Lumerical FDTD. Quantum efficiency QE can be calculated as the relation between the decay rates or the power as

$$\frac{QE}{QE^o} = \frac{\Gamma_{\text{rad}}}{\Gamma_{\text{rad}} + \Gamma_{\text{nrad}}} = \frac{P_{\text{rad}}}{P_{\text{rad}} + P_{\text{nrad}}} \quad (\text{S17})$$

where Γ_{nrad} and P_{nrad} is an additional nonradiative decay rate of the transition in the emitter and the power absorbed by the antenna only. By assuming the emitter has a high intrinsic QE , therefore the QE^o is equal to 100 % and $\Gamma_{\text{nr}}^o = 0$. So that

$$QE = \frac{\Gamma_{\text{rad}}}{\Gamma_{\text{rad}} + \Gamma_{\text{nrad}}} = \frac{P_{\text{rad}}}{P_{\text{rad}} + P_{\text{nrad}}} \quad (\text{S18})$$

TABLE S1. **Comparison of room temperature time-resolved photo- and X-ray luminescence fitting parameters.** Where τ_i (for $i = 1, 2$ and 3), $\bar{\tau}$, Γ and Γ/Γ_0 corresponds to i -th decay component, mean decay time, decay rate and relative decay rate, respectively. Percentages correspond to the i -th decay contribution.

	PL			XL		
	CsPbBr ₃	CsPbBr ₃ +Ag SNPs	CsPbBr ₃ + Ag CNPs	CsPbBr ₃	CsPbBr ₃ +Ag SNPs	CsPbBr ₃ + Ag CNPs
τ_1 (ns)	0.99 ± 0.03 (42.6%)	0.71 ± 0.05 (76.0%)	0.61 ± 0.04 (89.1%)	0.71 ± 0.01 (22.1%)	0.70 ± 0.03 (45.8%)	0.67 ± 0.04 (52.1%)
τ_2 (ns)	6.28 ± 0.07 (57.4%)	4.46 ± 0.12 (24.0%)	3.71 ± 0.15 (10.1%)	3.16 ± 0.04 (48.5%)	3.05 ± 0.09 (38.0%)	2.91 ± 0.07 (30.9%)
τ_3 (ns)	-	-	-	20.01 ± 0.31 (29.4%)	16.62 ± 0.41 (16.2%)	14.53 ± 0.33 (17.0%)
$\bar{\tau}$ (ns)	4.02 ± 0.13	1.61 ± 0.08	0.94 ± 0.06	7.55 ± 0.12	4.18 ± 0.13	3.71 ± 0.09
Γ (1/s)	0.25 ± 0.01	0.62 ± 0.01	1.05 ± 0.02	0.13 ± 0.01	0.24 ± 0.01	0.27 ± 0.01
Γ/Γ_0	1.00 ± 0.01	2.48 ± 0.17	4.20 ± 0.31	1.00 ± 0.01	1.84 ± 0.07	2.08 ± 0.06

CALCULATION OF COUPLED CSPBBR₃ NCS ON AG NP SURFACES

An analysis of the overlap between energy-dispersive X-ray spectroscopy (EDS) images for Ag and Pb or Br elements was conducted using the Sørensen-Dice index (SDI)^{43,62–64}, following the conversion of the images to black-and-white scale. This analysis incorporated size approximations of Ag nanocubes and CsPbBr₃ NPs. The percentage of coupled CsPbBr₃ NPs with Ag was derived from the averages of 8 overlap mappings between Ag and the Pb or Br elements. Thus, the coupling percentage C_{coup} can be calculated as⁶⁴:

$$C_{coup} = \text{SDI} \times 100\% = \frac{2|A_{Ag} \cap A_{Pb,Br}|}{|A_{Ag}| + |A_{Pb,Br}|} \times 100\% \quad (\text{S19})$$

where $|A_{Ag}|$ and $|A_{Pb,Br}|$ are the cardinalates between Ag atomic sets and Pb or Br atomic sets.

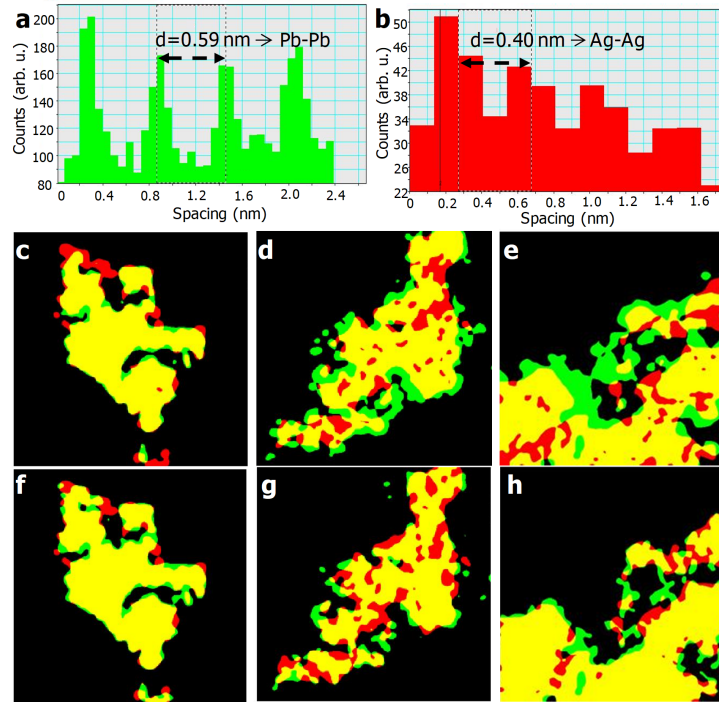


FIG. S3. **STEM HAADF and EDS images.** **a,b**, The atomic distances of Pb-Pb (**a**) and Ag-Ag (**b**), extracted from the STEM-HAADF images with Digital Micrograph software. **c-h** EDS images of Ag-Br (**c-e**) and Ag-Pb (**f-h**) overlaps. The red, green, and yellow colour corresponds to Ag, Pb, or Br atoms. The overlap area is derived from SDI.

QUANTUM EFFICIENCY, PL QUANTUM YIELD, AND ITS RELATIONSHIP TO THE PURCELL ENHANCEMENTS

PL quantum yield measurements were used to estimate QE . The measurements were performed using an Integration Sphere Assembly F-M01 (Edinburgh Instruments) with FLS980 spectrofluorimeter. Xenon lamp was used as an excitation source, with 375 nm wavelength selection. From several measurements, we found that the PLQY is about $55 \pm 15 \%$. This is still similar with the previous report of 64% ⁴⁶.

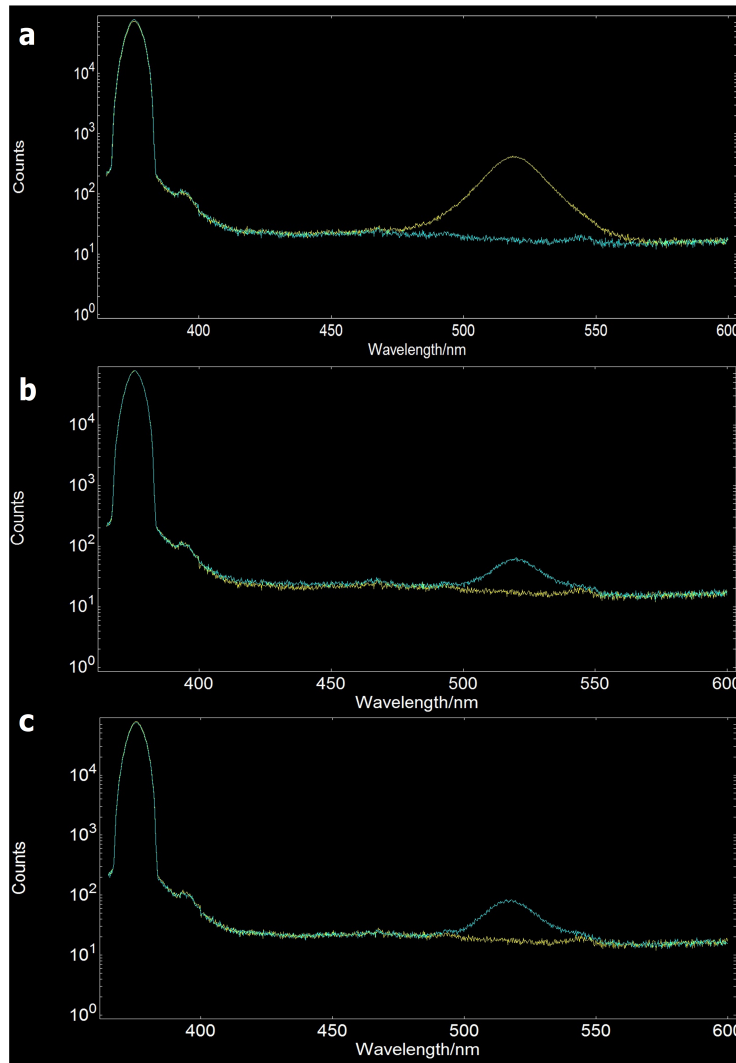


FIG. S4. Measured Toluene reference and photoluminescence spectra for determination of quantum efficiencies. a-c, Spectra collected from CsPbBr₃ (a), CsPbBr₃ + Ag SNPs (b), and CsPbBr₃ + Ag CNPs (c).

From the measurements above, we obtain QE of $(55 \pm 15) \%$. Such QE value has effects for both intensity P and emission rate Γ enhancements. Both cases are related with the contributions of radiative Γ_{rad} and non-radiative Γ_{nrad} and they can be written as

$$QE = \frac{\Gamma_{rad}}{\Gamma_{tot}} = \frac{\Gamma_{rad}}{\Gamma_{rad} + \Gamma_{nrad}} \quad (\text{S20})$$

where Γ_{tot} is the total decay rate. For bare CsPbBr₃ NC in PDMS system (denoted by superscript "o"), we can obtain the following relationship:

$$\frac{\Gamma_{nrad}^o}{\Gamma_{rad}^o} = \frac{1}{QE} - 1 \quad (\text{S21})$$

The enhancements of total decay rate in the CsPbBr₃-AgNP scintillator (denoted by superscript "np") system, η_{dec} , can be written as

$$\eta_{dec} = \frac{\Gamma_{tot}^{np}}{\Gamma_{tot}^o} = \frac{\Gamma_{rad}^{np} + \Gamma_{nrad}^{np}}{\Gamma_{rad}^o + \Gamma_{nrad}^o} \quad (\text{S22})$$

The enhancements of intensity, η_{int} , can be written as

$$\eta_{int} = \frac{QE^{np}}{QE^o} = \frac{\Gamma_{rad}^{np}/\Gamma_{rad}^o}{\eta_{dec}} \quad (\text{S23})$$

Then we can obtain the enhancement of radiative decay rate ($\Gamma_{rad}^{np}/\Gamma_{rad}^o$) as

$$\frac{\Gamma_{rad}^{np}}{\Gamma_{rad}^o} = \eta_{int} \times \eta_{dec} \quad (\text{S24})$$

By simplifying the expression of η_{dec} , we can obtain the enhancement of non-radiative decay rate, ($\Gamma_{nrad}^{np}/\Gamma_{nrad}^o$), as

$$\frac{\Gamma_{nrad}^{np}}{\Gamma_{nrad}^o} = \eta_{dec} \frac{(1/QE^o) - \eta_{int}}{(1/QE^o) - 1} \quad (\text{S25})$$

The coupling with a plasmon can lead to enhancements in both radiative decay and non-radiative decay. For a high QE system ($QE \approx 100 \%$), which means the total decay rate is dominated by the radiative decay rate, i.e. $\Gamma_{tot} \approx \Gamma_{rad}$. We can observe the enhancement of radiative decay rate, $\Gamma_{rad}^{np}/\Gamma_{rad}^o$, from the time-resolved PL measurements, while it is difficult to observe the enhancement of non-radiative decay rate, $\Gamma_{nrad}^{np}/\Gamma_{nrad}^o$. The emission efficiency thus will not be greatly enhanced since QE is already close to 100 %. For a low QE system ($QE \ll 100\%$), i.e. $\Gamma_{tot} \approx \Gamma_{nrad}$. We can observe the enhancement of non-radiative decay rate from time-resolved PL measurements, while it is hard to observe the enhancement of radiative decay rate. In our case, the QE of $55 \pm 15 \%$ enables us

to observe both enhancements in radiative decay and non-radiative decay when the dipole emission is coupled to the plasmon. The 5-nm polyvinylpyrrolidone (PVP) layer assures that $\Gamma_{rad}^{mp}/\Gamma_{rad}^o \gg \Gamma_{nrad}^{mp}/\Gamma_{nrad}^o$.

Regarding the Purcell factor (F_p) from Eqs. S7, S8, S9, and S12, we can obtain the corrected Purcell factor (F_p^{corr}) for our samples (with many CsPbBr₃ NCs coupled to many Ag NPs) as following:

$$F_p^{corr} \approx QE \times C_{coup} \times F_p \quad (\text{S26})$$

where in our case, QE of $(55 \pm 15)\%$ and C_{coup} of $(70 \pm 8)\%$ resulting $F_p^{corr} \approx (39 \pm 17)\%F_p$.

TEMPERATURE-DEPENDENT PHOTO- AND X-RAY LUMINESCENCE MEASUREMENTS

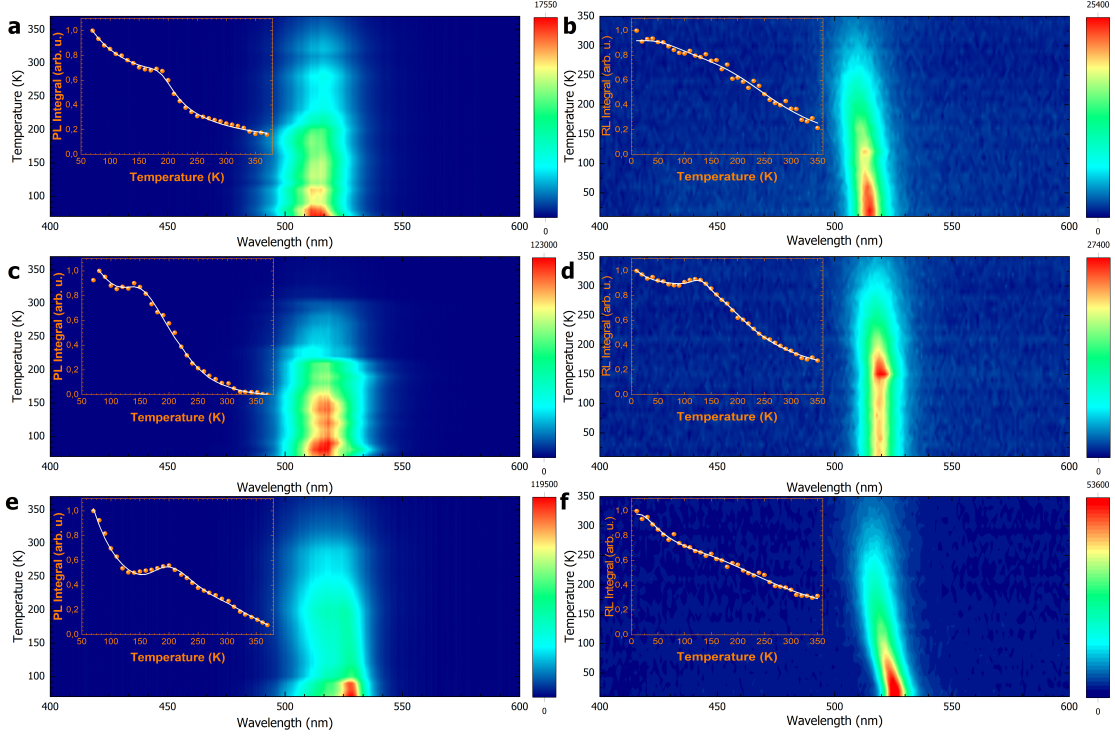


FIG. S5. Temperature-dependent photo- and X-ray luminescence spectra of samples. **a-f**, Spectral maps of photo- and X-ray luminescence of CsPbBr₃ (**a** and **b**, respectively), CsPbBr₃ + Ag SNPs (**c** and **d**, respectively) and CsPbBr₃ + Ag CNPs (**e** and **f**, respectively). Insets represent an integrated area under each luminescence alongside the NTQ fitting curve.

All samples, pure and Ag NPs-doped revealed a negative thermal quenching (NTQ) behaviour, which was fit using Shibata's model⁶⁵. All essential parameters and spectra are presented in Supporting Tables S2 and S3 and Supporting Fig. S5.

TABLE S2. **Analysis of temperature-dependent X-ray luminescence spectra.** X-ray luminescence negative thermal quenching model fitting parameters.

	CsPbBr ₃	CsPbBr ₃ + Ag SNPs	CsPbBr ₃ + Ag CNPs
C ₁	$1.1 \cdot 10^0$	$6.6 \cdot 10^1$	$9.2 \cdot 10^{-1}$
E ₁ ^D (meV)	19.9	27.9	8.09
C ₂	$8.9 \cdot 10^1$	$1.8 \cdot 10^3$	$2.6 \cdot 10^1$
E ₂ ^D (meV)	113	87	84
D ₁	-	$1.1 \cdot 10^2$	-
E ₃ ^N (meV)	-	33	-

TABLE S3. **Analysis of temperature-dependent photoluminescence spectra.** Photoluminescence negative thermal quenching model fitting parameters.

	CsPbBr ₃	CsPbBr ₃ + Ag SNPs	CsPbBr ₃ + Ag CNPs
C ₁	$1.9 \cdot 10^0$	$1.8 \cdot 10^0$	$2.5 \cdot 10^1$
E ₁ ^D (meV)	6.95	4.05	30.4
C ₂	$6.8 \cdot 10^5$	$2.6 \cdot 10^5$	$1.6 \cdot 10^6$
E ₂ ^D (meV)	230	206	249
C ₃	$2.6 \cdot 10^8$	$7.6 \cdot 10^8$	$8.9 \cdot 10^8$
E ₃ ^D (meV)	403	404	428
D ₁	$5.1 \cdot 10^1$	$4.2 \cdot 10^1$	$5.4 \cdot 10^1$
E ₁ ^N (meV)	95.7	89.7	54.7

LOW-TEMPERATURE THERMOLUMINESCENCE

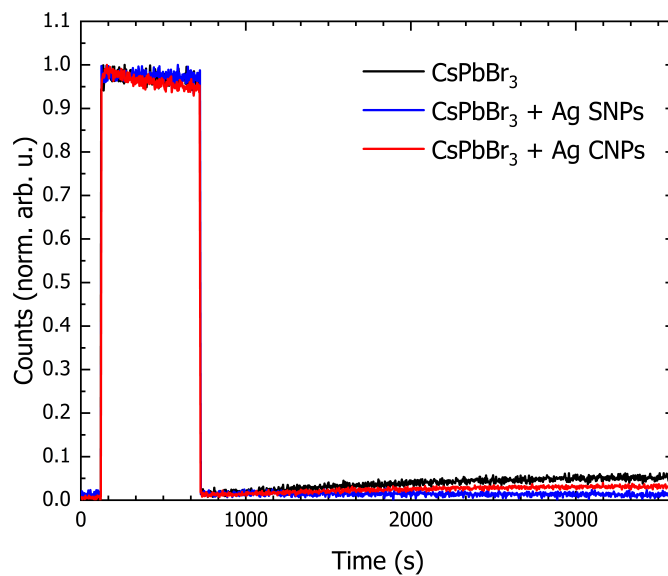


FIG. S6. **Thermoluminescence measurements.** Comparison of low-temperature thermoluminescence curves of pure CsPbBr₃, Ag SNPs-doped, and Ag CNPs-doped samples.

X-RAY IMAGING

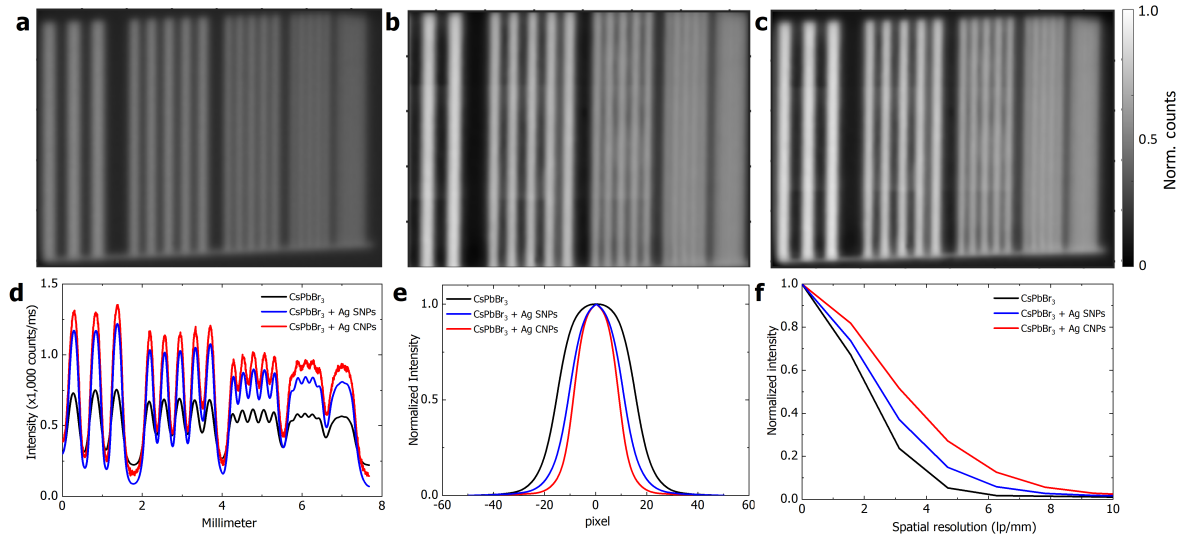


FIG. S7. **X-ray imaging using a resolution card a-c**, X-ray images employing resolution card type 18a of CsPbBr₃ (a), CsPbBr₃ + Ag SNPs (b), and CsPbBr₃ + Ag CNPs (c). **d**, Cross sections of card imaging. **e,f**, Line Spread Function (e), and Modulation Transfer Function (MTF) (f) of square X-ray imaging in Figs. 5a-5c.

TABLE S4. **Spatial resolution (lp/mm) at 0.2MTF**. The parameters derived from Figs. 5a-5c in the main manuscript after calculating edge and line spread functions with Fourier transform.

Sample	Spatial resolution (lp/mm) at 0.2 MTF
CsPbBr ₃	3.44
CsPbBr ₃ + Ag SNPs	4.35
CsPbBr ₃ + Ag CNPs	5.47

PULSE HEIGHT SPECTRA

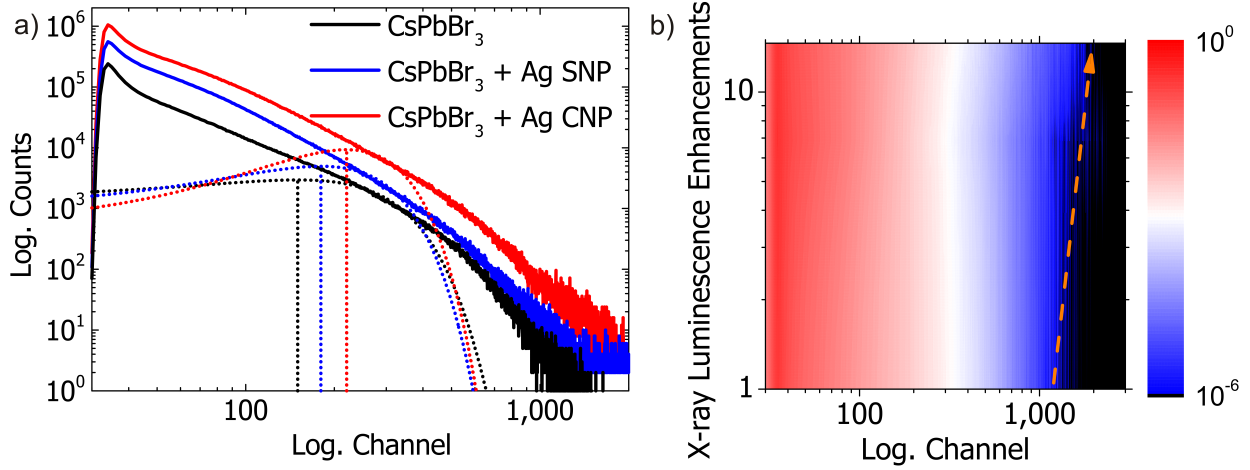


FIG. S8. **Pulse height spectra.** **a**, Pulse height spectra of various PDMS samples irradiated with ^{241}Am , including CsPbBr₃ NCs, CsPbBr₃ NCs with Ag SNPs, and CsPbBr₃ NCs with Ag CNPs. Gaussian fits are overlaid on the pulse height spectra, with dashed lines indicating the fit curves and peak positions. **b**, A surface plot depicts the pulse height spectra as a function of the X-ray luminescence enhancement in Figs. 4 and 5, showcasing a pronounced long tail in the spectrum of CsPbBr₃ NCs with Ag CNPs, see orange arrow. While clear photopeaks are not distinctly visible, calculated enhancement factors from both methods in **a** and **b**) of 1.20 ± 0.15 for samples with Ag SNPs and 1.47 ± 0.39 for those with Ag CNPs.

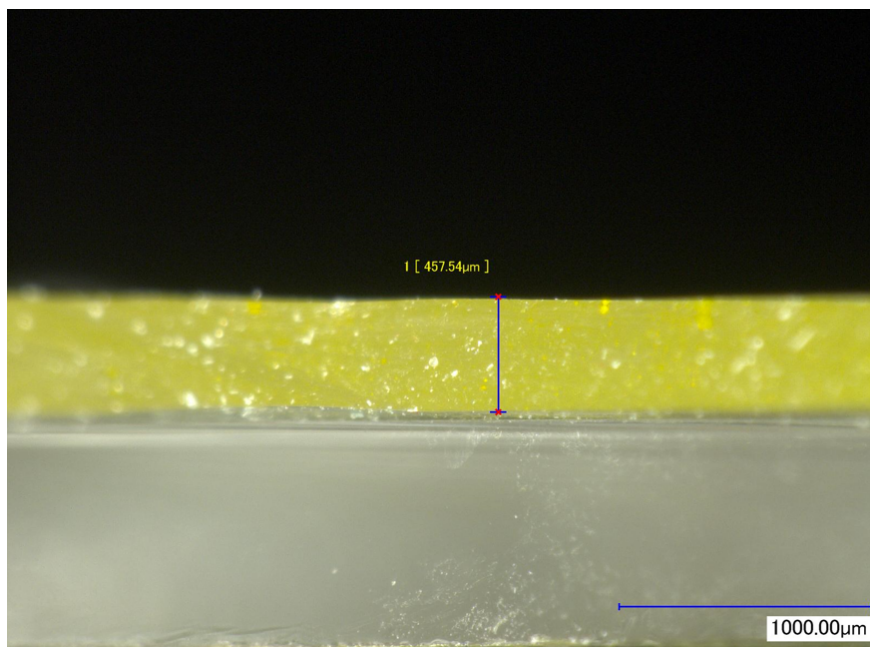


FIG. S9. **Samples for X-ray imaging.** Cross-section of $\text{CsPbBr}_3 + \text{Ag}$ CNPs doped samples in a layer form, taken under Keyence microscope.

REFERENCES

- ¹Lecoq, P. Development of new scintillators for medical applications. *Nucl. Instruments Methods Phys. Res. Sect. A Accel. Spectrometers, Detect. Assoc. Equip.* **809**, 130–139 (2016).
- ²Farnworth, A. & Bugby, S. Intraoperative gamma cameras: a review of development in the last decade and future outlook. *J. Imaging Sci. Technol.* **9**, 102–138 (2023).
- ³Weber, M. J. Inorganic scintillators: today and tomorrow. *J. Lumin.* **100**, 35–45 (2002).
- ⁴Wiggins, B. *et al.* Scintillation properties of semiconducting ⁶LiInSe₂ crystals to ionizing radiation. *Nucl. Instrum. Methods Phys. Res. Sect. A.* **801**, 73–77 (2015).
- ⁵Lei, L. *et al.* Next generation lanthanide doped nanoscintillators and photon converters. *eLight* **2**, 17–40 (2022).
- ⁶Hofstadter, R. The detection of gamma-rays with thallium-activated sodium iodide crystals. *Phys. Rev.* **75**, 796–810 (1949).
- ⁷Xie, A. *et al.* Thermal Quenching and Dose Studies of X-ray Luminescence in Single Crystals of Halide Perovskites. *J. Phys. Chem. C* **122**, 16265–16273 (2018).
- ⁸Chen, Q. *et al.* All-inorganic perovskite nanocrystal scintillators. *Nature* **561** (2018).
- ⁹Roques-Carmes, C. *et al.* A framework for scintillation in nanophotonics. *Science* **375**, eabm9293 (2022).
- ¹⁰Martin-Monier, L. *et al.* Large-scale self-assembled nanophotonic scintillators for x-ray imaging (2024). 2410.07141.
- ¹¹Ye, W. *et al.* The Nanoplasmonic Purcell Effect in Ultrafast and High-Light-Yield Perovskite Scintillators. *Adv. Mater.* **36**, 2309410 (2024).
- ¹²Delgado, H. C., Moradifar, P., Chinn, G., Levin, C. S. & Dionne, J. A. Toward "super-scintillation" with nanomaterials and nanophotonics. *Nanophot.* **13**, 1953–1962 (2024).
- ¹³Purcell, E. Spontaneous emission probabilities at radio frequencies. *Phys. Rev.* **69**, 681 (1946).
- ¹⁴Kurman, Y., Shultzman, A., Segal, O., Pick, A. & Kaminer, I. Photonic-Crystal Scintillators: Molding the Flow of Light to Enhance X-Ray and γ -Ray Detection. *Phys. Rev. Lett.* **125**, 040801 (2020).
- ¹⁵Kurman, Y. *et al.* Purcell-enhanced X-ray scintillation. *Appl. Phys.* **arXiv:2302.01300v2** (2023).

- ¹⁶Krivenkov, V., Samokhvalov, P., Nabiev, I. & Rakovich, Y. P. Synergy of Excitation Enhancement and the Purcell Effect for Strong Photoluminescence Enhancement in a Thin-Film Hybrid Structure Based on Quantum Dots and Plasmon Nanoparticles. *J. Phys. Chem. Lett.* **11**, 8018–8025 (2020).
- ¹⁷Melcher, C. Scintillation Crystals for PET. *J. Nucl. Med.* **41**, 1051–1055 (2000).
- ¹⁸Birowosuto, M. D. *et al.* X-Ray Scintillation in Lead Halide Perovskite Crystals. *Sci. Rep.* **6**, 37254 (2016).
- ¹⁹Xie, A. *et al.* Thermal Quenching and Dose Studies of X-Ray Luminescence in Single Crystals of Halide Perovskites. *J. Phys. Chem.* **C122**, 16265–16273 (2018).
- ²⁰Xie, A. *et al.* Library of Two-Dimensional Hybrid Lead Halide Perovskite Scintillator Crystals. *Chem. Mater.* **32**, 8530–8539 (2020).
- ²¹Gandini, M. *et al.* Efficient, fast and reabsorption-free perovskite nanocrystal-based sensitized plastic scintillators. *Nat. Nanotechnol.* **15**, 462–468 (2020).
- ²²Mi, Z. *et al.* Real-time single-proton counting with transmissive perovskite nanocrystal scintillators. *Nat. Mater.* **23**, 803–809 (2024).
- ²³Yang, Z., Yao, J., Xu, L., Fan, W. & Song, J. Designer bright and fast csppbr3 perovskite nanocrystal scintillators for high-speed x-ray imaging. *Nat. Commun.* **15**, 1–10 (2024).
- ²⁴Carminati, R. *et al.* Electromagnetic density of states in complex plasmonic systems. *Surf. Sci. Rep.* **70**, 1–41 (2015).
- ²⁵El-Dardiry, R. G. S., Faez, S. & Lagendijk, A. Classification of light sources and their interaction with active and passive environments. *Phys. Rev. A* **83**, 031801 (2011).
- ²⁶Birowosuto, M. D. *et al.* Movable high-q nanoresonators realized by semiconductor nanowires on a si photonic crystal platform. *Nat. mater.* **13**, 279–285 (2014).
- ²⁷Birowosuto, M. D., Skipetrov, E., S., Vos, W. L. & Mosk, A. Observation of spatial fluctuations of the local density of states in random photonic media. *Phys. Rev. Lett.* **105**, 013904 (2010).
- ²⁸Krachmalnicoff, V., Castanié, E., De Wilde, Y. & Carminati, R. Fluctuations of the local density of states probe localized surface plasmons on disordered metal films. *Phys. Rev. Lett.* **105**, 183901 (2010).
- ²⁹Sapienza, R. *et al.* Long-tail statistics of the purcell factor in disordered media driven by near-field interactions. *Phys. Rev. Lett.* **106**, 163902 (2011).

- ³⁰Peng, P. *et al.* Enhancing coherent light-matter interactions through microcavity-engineered plasmonic resonances. *Phys. Rev. Lett.* **119**, 233901 (2017).
- ³¹Frimmer, M. & Koenderink, A. F. Spontaneous emission control in a tunable hybrid photonic system. *Phys. Rev. Lett.* **110**, 217405 (2013).
- ³²Koenderink, A. F. On the use of purcell factors for plasmon antennas. *Opt. Lett.* **35**, 4208–4210 (2010).
- ³³Ruppin, R. Electromagnetic energy density in a dispersive and absorptive material. *Physics Letters A* **299**, 309–312 (2002).
- ³⁴Bowen, P. T. & Smith, D. R. Coupled-mode theory for film-coupled plasmonic nanocubes. *Phys. Rev. B* **90**, 195402 (2014).
- ³⁵Ruppin, R. Decay of an excited molecule near a small metal sphere. *J. Chem. Phys.* **76**, 1681 (1982).
- ³⁶Chew, H. Transition rates of atoms near spherical surfaces. *J. Chem. Phys.* **87**, 1335 (1987).
- ³⁷Wibowo, A. *et al.* Development and challenges in perovskite scintillators for high-resolution imaging and timing applications. *Commun. Mater.* **4** (2023).
- ³⁸Hou, S. *et al.* Manipulating Coherent Light-Matter Interaction: Continuous Transition between Strong Coupling and Weak Coupling in MoS₂ Monolayer Coupled with Plasmonic Nanocavities. *Adv. Opt. Mater.* **7**, 1900857 (2019).
- ³⁹Yu, J. *et al.* Electrically control amplified spontaneous emission in colloidal quantum dots. *Sci. Adv.* **5**, eaav3140 (2019).
- ⁴⁰Mahato, S. *et al.* Surface-Engineered Methylammonium Lead Bromide Single Crystals: A Platform for Fluorescent Security Tags and Photodetector Applications. *Adv. Opt. Mater.* **12**, 1–11 (2024).
- ⁴¹Mahato, S. *et al.* Atomic-Scale Imaging and Nano-Scale Mapping of Cubic α -CsPbI₃ Perovskite Nanocrystals for Inverted Perovskite Solar Cells. *ACS Appl. Mater. Interfaces* **14**, 9711–9723 (2022).
- ⁴²Huang, Q. *et al.* Enhancing crystal integrity and structural rigidity of cspbbr₃ nanoplatelets to achieve a narrow color-saturated blue emission. *Light Sci. Appl.* **13** (2024).
- ⁴³Balaur, E. *et al.* Colorimetric histology using plasmonically active microscope slides. *Nature* **598**, 65–71 (2021).

- ⁴⁴Leistikow, M. D., Johansen, J., Kettelarij, A. J., Lodahl, P. & Vos, W. L. Size-dependent oscillator strength and quantum efficiency of cdse quantum dots controlled via the local density of states. *Phys. Rev. B* **79**, 045301 (2009).
- ⁴⁵Raza, S., Bozhevolnyi, S. I., Wubs, M. & Mortensen, N. A. Nonlocal optical response in metallic nanostructures. *J. Phys.: Condens. Matter* **27**, 183204 (2015).
- ⁴⁶Maddalena, F. *et al.* Stable and Bright Commercial CsPbBr₃ Quantum Dot-Resin Layers for Apparent X-ray Imaging Screen. *ACS Appl. Mater. Interfaces*. **13**, 59450–59459 (2021).
- ⁴⁷Coenen, T., Arango, F. B., Koenderink, A. F. & Polman, A. Directional emission from a single plasmonic scatterer. *Nat. Commun.* **5**, 3250 (2014).
- ⁴⁸Baravaglio, M. *et al.* Energy deposition in liquid scintillators composed of cspbbr3 colloidal nanocrystal dispersions. *Nanoscale* **16**, 17176–17186 (2024).
- ⁴⁹Payne, S. A. *et al.* Nonproportionality of scintillator detectors: Theory and experiment. *IEEE Trans. Nucl. Sci.* **56**, 2506–2512 (2009).
- ⁵⁰Jin, T. *et al.* Self-wavelength shifting in two-dimensional perovskite for sensitive and fast gamma-ray detection. *Nat. Commun.* **14**, 2808 (2023).
- ⁵¹Zhang, Y. *et al.* Metal Halide Perovskite Nanosheet for X-ray High-Resolution Scintillation Imaging Screens. *ACS Nano* **13**, 2520–2525 (2019).
- ⁵²Bignell, L. J., Mume, E., Jackson, T. W. & Lee, G. P. Plasmonic light yield enhancement of a liquid scintillator. *Appl. Phys. Lett.* **102**, 211902 (2013).
- ⁵³Marie-Luce, R. *et al.* Real-time detection and discrimination of radioactive gas mixtures using nanoporous inorganic scintillators. *Nat. Phot.* (2024).
- ⁵⁴Orfano, M. *et al.* Efficient radioactive gas detection by porous metal-organic framework scintillating nanocrystals. *Nat. Phot.* **17**, 672–678 (2023).
- ⁵⁵Palik, E. *Handbook of Optical Constants of Solids* (Elsevier, 1997).
- ⁵⁶Sortino, L. *et al.* Optically addressable spin defects coupled to bound states in the continuum metasurfaces. *Nat. Commun.* **15**, 2008 (2024).
- ⁵⁷Akselrod, G. M. *et al.* Probing the mechanisms of large Purcell enhancement in plasmonic nanoantennas. *Nat. Photonics* **8**, 1–6 (2014).
- ⁵⁸Ghorai, A., Mahato, S., Srivastava, S. K. & Ray, S. K. Atomic Insights of Stable, Monodispersed CsPbI_{3-x}Br_x (x = 0, 1, 2, 3) Nanocrystals Synthesized by Modified Ligand Cell. *Adv. Funct. Mater.* **32**, 62202087 (2022).

- ⁵⁹Bowen, P. & Smith, D. Coupled-mode theory for film-coupled plasmonic nanocubes. *Phys. Rev. B* **90**, 195402 (2014).
- ⁶⁰Ito, K., Watari, T., Nishikawa, K., Yoshimoto, H. & Iizuka, H. Quasi-analytic study of scattering from optical plasmonic patch antennas. *J. Appl. Phys.* **114**, 16103 (2013).
- ⁶¹Hung, L., Lee, S. Y., McGovern, O., Rabin, O. & Mayergoyz, I. Calculation and measurement of radiation corrections for plasmon resonances in nanoparticles. *Phys. Rev. B* **88**, 075424 (2013). URL <https://link.aps.org/doi/10.1103/PhysRevB.88.075424>.
- ⁶²Sørensen, T. A method of establishing groups of equal amplitude in plant sociology based on similarity of species and its application to analyses of the vegetation on Danish commons. *KDVS* **5**, 1–34 (1948).
- ⁶³Dice, L.R. Measures of the Amount of Ecologic Association Between Species. *Ecology* **26**, 297–302 (1945).
- ⁶⁴Carass, A. *et al.* Evaluating white matter lesion segmentations with refined sørensen-dice analysis. *Sci. Rep.* **10**, 8242 (2020).
- ⁶⁵Shibata, H. Negative Thermal Quenching Curves in Photoluminescence of Solids. *Jpn. J. Appl. Phys.* **37**, 550 (1998).